J. Fluid Mech. (2002), *vol.* 458, *pp.* 333–377. © 2002 Cambridge University Press
DOI: 10.1017/S0022112002007863 Printed in the United Kingdom

Response of turbulent boundary layers to multiple strain rates

By A. C. SCHWARZ†, M. W. PLESNIAK‡ AND S. N. B. MURTHY

Purdue University, School of Mechanical Engineering, Maurice J. Zucrow Laboratories,
West Lafayette, IN 47907-1003, USA

(Received 8 July 1999 and in revised form 30 October 2001)

Many practical applications, such as in blade cascades and turbomachinery, involve inhomogeneous turbulent shear flows subjected simultaneously to multiple strains. In principle, the applied strain can be combined to yield an effective strain. However, no simple stress–strain relation is capable of establishing turbulent stress or energy balance in the mean or on an instantaneous basis. In the current investigation, a turbulent boundary layer is examined in the presence of convex curvatures of different strengths combined with streamwise (favourable and adverse) pressure gradients, with various values of pressure gradient ratio, $(\partial P/\partial s)/(\partial P/\partial n)$. Measurements of the mean and turbulent parameters and flux Richardson number show appreciable changes, mainly in the outer portion of the boundary layer ($y^+ > 100$). The turbulent burst frequency, particularly at the location of application of the additional strain rate, also changes relative to its value with wall curvature alone.

Three primary observations from these experiments are as follows: (i) in all cases, the mean velocity profile and all of the measured Reynolds stresses collapse in the near-wall region using standard inner scaling; (ii) the applied strains combine nonlinearly, with one of the strains dominating the local flow during its development; (iii) the ratio of the radial to axial pressure gradient magnitude influences both classical turbulence correlations and mean flow, as well as the physical production cycle of turbulence; and (iv) application rate of newly introduced strain rates is at least as important as their magnitudes.

1. Introduction

Many practical flows of engineering interest are influenced by multiple, interacting strains. Because of curved surfaces, low-aspect-ratio passages, and streamwise and spanwise strains, the momentum and heat transfer mechanisms in turbomachinery are highly complex. In figure 1, a diagram of a typical blade passage section is shown to point out essential geometrical features, i.e. the surface curvatures, the leading edge of the blade, and the changes in the cross-sectional area between the blades. Other complexities are due to endwall effects and rotation. However, even in the simplest case of a curved wall diffusing passage, the combination of strain rates can be expected to affect the turbulence in the flow to an extent that requires attention

---

† Current address: Caterpillar Inc., Corporate Information Services, AD 3335, 600 W. Washington Street, East Peoria, IL 61630-3335, USA.

‡ Author to whom correspondence should be addressed: plesniak@ecn.purdue.edu.

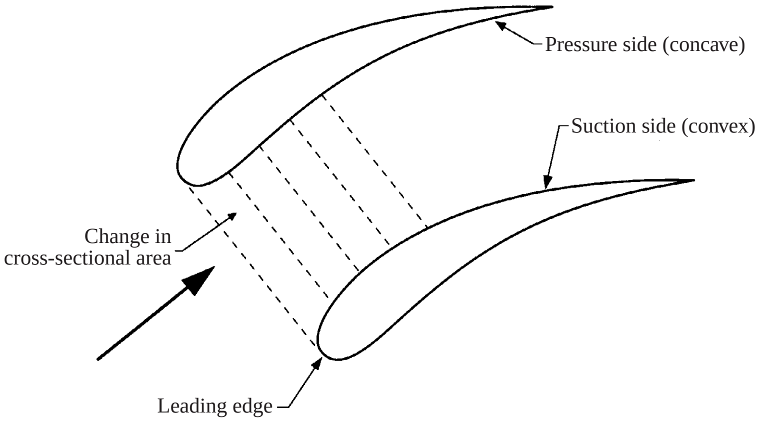

Figure 1. Diagram of typical flow passage in turbomachinery.

in design. With the desire to achieve better performance, durability and economy in turbomachines, it has become increasingly important to understand the fundamental mechanisms of momentum and heat transfer.

Extra strain rate effects on the structure of a two-dimensional turbulent boundary layer (TBL) have received considerable attention over the past two decades. A number of workers have performed experiments to study the influence of additional rates of strain, e.g. convex and concave curvature (cf. So & Mellor 1973; Gillis & Johnston 1983; Muck, Hoffman & Bradshaw 1985; Barlow & Johnston 1988*a*, *b*), as well as adverse and favourable streamwise pressure gradients (e.g. Kline *et al.* 1967; Narasimha & Sreenivasan 1979; White & Tiederman 1990; Nagano, Tagawa & Tsuji 1991; Fernholz & Warnack 1998).

However, there have been relatively few studies addressed at examining multiple strain rate interactions in turbulent flows. Consequently, detailed experimental studies of the initial response and downstream development of a TBL exposed to multiple strain rates are warranted.

It is well-established that, in the Reynolds-averaged framework, the turbulent shear stress is not directly affected by mean pressure gradients because no pressure gradient terms appear explicitly in the Reynolds stress transport equations (Bradshaw 1973, 1994). There is, in fact, no production term in the transport equation for primary Reynolds shear stress, $-\overline{uv}$, due to mean pressure gradient. However, curvature not only introduces an additional term due to 'extra strain', U/R, but affects the main production term in the turbulent kinetic energy equation through its dramatic effect on shear stress. The main contribution of the strain rate associated with streamwise pressure gradient in the turbulent kinetic energy equation is through a 'normal stress production' term, Baskaran, Smits & Joubert (1991). The results of our study demonstrate that the imposed streamwise strain rate (combined with curvature), and its rate of application, has a significant effect on turbulence quantities. This suggests that, in such cases, the Reynolds stress evolution equations give an incomplete description of the flow. Several alternative formulations have been proposed including: the rapid distortion theory approach (see Savill 1987), the large eddy interaction model (LEIM) of Hong & Murthy (1986*a*) for curved flows, and the structure-based model of Reynolds & Kassinos (1995) for rotating flows.

1.1. *Effects of single extra strain rates*

The effects of longitudinal curvature have been studied extensively over the past few decades (see the comprehensive literature review by Patel 1997). The early experiments of So & Mellor (1973) and Gillis & Johnston (1983) found that the primary Reynolds shear stress was diminished in the outer region of the turbulent boundary layer. In both studies, a zero streamwise pressure gradient was maintained over most of the convex wall by carefully contouring the opposite wall, except immediately downstream of the onset of curvature, where a favourable pressure gradient prevailed locally. Effects of this locally strong acceleration, and its application rate, on the turbulence structure were not accounted for in either study.

The applicability of the 'log-law' in TBLs with one or more extra rates-of-strain has been widely discussed. In a comprehensive study by Gibson (1988) on the effects of surface curvature, it was shown that the logarithmic region existed for the mean streamwise velocity component, wherein the 'log-law' constants could be different from the standard values (1/0.41 for the slope and 5.0 for the intercept). Gibson (1988) suggested a value of 5.78 for the intercept, while the von Kármán constant remained unchanged. A more extensive discussion of this issue can be found in Schwarz & Plesniak (1996*b*).

The analogy between streamline curvature and buoyancy in turbulent shear flow was first discussed by Bradshaw (1969). This analogy between the two phenomena turned out to be a good first approximation, based on the close correlation between temperature fluctuations and streamwise velocity component fluctuations. Through the application of mixing-length calculations based upon meteorological data to curved shear layers, the predicted effects of streamline curvature were surprisingly large, e.g. 10% change in mixing length in a boundary layer with $\delta/R \approx \frac{1}{300}$. The flux Richardson number, Ri_{fl}, for curved flows is defined as the ratio of the energy transfer rate from transverse (wall-normal) velocity fluctuations to the total energy transfer rate from the mean flow (Townsend 1976)

$$Ri_{fl} = \frac{2\overline{uv}\bar{U}/r}{(\overline{uv}/r)(\partial/\partial n)(\bar{U}r)} = \frac{2S_{rad}}{1+S_{rad}}, \tag{1}$$

where S_{rad} is the strain rate ratio, or curvature parameter, of the mean flow. For a turbulent flow with convex streamlines, an increase in the flux Richardson number is associated with an increased stabilization of the TBL. In stratified boundary layers, considerable changes in the velocity profiles were observed when the flux Richardson number exceeded 0.05 (Townsend 1976).

Spalart & Shur (1997) and Shur *et al.* (2000) proposed and evaluated an eddy-viscosity turbulence model that accounts for system rotation and streamline curvature. Their proposal of a Galilean-invariant quantity to replace $-\bar{U}/r$ led to an expression for the Lagrangian derivative of the angle of the strain-rate principal axis, α_{SR}. The principal axes angles for both the strain-rate tensor, α_{SR}, and the Reynolds tensor, α_{ReS}, for a two-dimensional mean flow can be calculated from:

$$\alpha_{SR} = \tfrac{1}{2}\,\mathrm{atan}\left[\frac{-2S_{sn}}{S_{nn}-S_{ss}}\right], \tag{2}$$

$$\alpha_{ReS} = -\tfrac{1}{2}\,\mathrm{atan}\left[\frac{-2\overline{uv}}{\overline{u^2}-\overline{v^2}}\right]. \tag{3}$$

The wall-normal diagonal strain-rate component, S_{nn}, can be determined from the measurements of the wall-normal velocity, $\bar{V}$, whereas the streamwise diagonal strain-rate component, S_{ss} can be inferred using the continuity equation for the (s, n)-coordinate system according to

$$\frac{\partial \bar{U}}{\partial s} \approx -\frac{\partial}{\partial n}\left[\bar{V}\left(1+\frac{n}{R}\right)\right]. \tag{4}$$

In this approximation, the spanwise derivative of the z-component of the mean velocity $(\bar{W})$ is neglected because of the two-dimensional mean flow assumption.

Holloway & Tavoularis (1998) also studied the effects of mild streamline curvature on anisotropy in sheared turbulence. They proposed a model which requires as inputs only the specification of turbulence anisotropies in a fully developed rectilinear reference flow, the geometrical features of the flow under study and a dimensionless mean eddy lifetime. The primary assumption is that the mean streamline curvature has no direct effect on the production and dynamics of each individual turbulent eddy.

The influence of extra strain rates arising from adverse and favourable streamwise pressure gradients has also been studied extensively. An adverse pressure gradient can destroy the logarithmic region and significantly change higher-order velocity moments as reported by Nagano *et al.* (1991), although it is unclear whether or not their turbulent boundary layer was in equilibrium. On the other hand, in cases of equilibrium boundary layers, the validity of the 'log-law' was established by White & Tiederman (1990) and Koskie (1991).

Narayanan & Ramjee (1969) reported that the breakdown of the 'logarithmic law' occurred at a value of the pressure gradient parameter $\Delta_P = (\nu/(\rho u_\tau^3))(\mathrm{d}P/\mathrm{d}s) \approx -0.02$, where ν is the kinematic viscosity and $\mathrm{d}P/\mathrm{d}s$ is the streamwise pressure gradient. This is associated with thickening of the linear sublayer, which occurs before the relaminarization of the mean velocity profiles and is a first sign of the onset of the reverse transition process.

In their review article, Narasimha & Sreenivasan (1979) describe the influence of highly accelerated flows (strong streamwise strain rate) on the mean statistics and turbulence structures in the boundary layer, especially the tendency of reversion to laminar flow caused by strong streamwise strain rates. They suggest a two-layer model, where the turbulence in the outer portion of the boundary layer is rapidly distorted and the Reynolds shear stress is nearly frozen. During this process, the viscous region exhibits random oscillations in response to the forcing provided by the remainder of the original turbulence. In this situation, reversion is a result of the slowly responding Reynolds stresses to the dominating pressure forces in the outer region, accompanied by the generation of a new laminar sub-boundary layer which is stabilized by the strong acceleration.

An adverse pressure gradient not only changes the force balance at the wall, but also rapidly produces an inflection point in the mean velocity profile. The latter causes rapid change in the outer-layer turbulence.

The influence of streamwise pressure gradients on near-wall 'low-speed streaks' in turbulent boundary layers has also been studied, cf. Kline *et al.* (1967). Adverse pressure gradients (APG) make bursting more frequent and violent, whereas favourable pressure gradients (FPG) reduce the bursting frequency, and, if the TBL is sufficiently accelerated ($k \approx 3.5 \times 10^{-6}$, where $k = (\nu/U_e^2)(\mathrm{d}U_e/\mathrm{d}s)$ is the acceleration parameter, and U_e is the streamwise velocity at the edge of the boundary layer), the bursting process ceases, leading to reverse transition and relaminarization. Thus, the streamwise pressure gradient can have a profound effect on the structure of the turbulence, if only indirectly.

1.2. *Effects of multiple extra strain rates*

Compared to the number of investigations of single extra strain rates, relatively few experimental studies concerning multiple pressure gradients have been conducted. In most of them, the individual strengths of the radial or streamwise pressure gradients were not controllable independently. Baskaran *et al.* (1987, 1991) studied the development of a TBL over a curved hill, which included extra strain rates due to curvature and axial pressure gradient, as well as reversal of curvature. Based on analysis of the Reynolds stress equations they concluded that the interaction between curvature and pressure gradient effects would be weak because the curvature affected primarily the shear stress, whereas the pressure gradient effects appeared mainly through the production of normal stresses.

The response of a TBL to multiple curvatures (convex and concave) and pressure gradients (favourable and adverse) was studied by Bandyopadhyay & Ahmed (1993) in an S-shaped duct. The formation of internal layers was detected at the convex curvature junctions. According to a criterion given by Baskaran *et al.* (1987), an internal layer grows when the curvature parameter $\Delta k^+ = \Delta R\nu/u_\tau > 0.373 \times 10^{-4}$, where $\Delta R = (1/R_2) - (1/R_1)$, R_1 and R_2 being the radii of curvature upstream and downstream of the onset of curvature, respectively. Bandyopadhyay & Ahmed (1993) also found that the effect of curvature dominates the accompanying sequences of streamwise pressure gradients. Furthermore, they found an asymmetric response of the TBL to concave and convex curvatures, i.e. the skin friction in the recovery region following curvature depended on the sequence of the curvature, concave–convex compared to convex–concave. No information was provided on Reynolds shear stresses, very near wall data, nor on the bursting process.

Webster, DeGraaff & Eaton (1996) examined a TBL over a surface bump experimentally, whereas Wu & Squires (1998) performed companion numerical studies using LES. The initially flat-plate zero-pressure-gradient TBL was subjected to alternating concave and convex curvature, as well as adverse and favourable pressure gradients. The surface discontinuity near the leading edge of the bump (concave to convex) triggered an internal layer, which rapidly grew because of a strong adverse pressure gradient. On the other hand, it was shown that the effect of convex curvature was small. Another noteworthy study is that by Chebbi, *et al.* (1998), in which the response of uniformly sheared, nearly homogeneous turbulence to changes in curvature was examined. The principal objective was to determine the rate of adjustment of the flow structure following stepwise changes in the mean curvature, e.g. transition from straight to curved section, curvature reversal, and relaxation from curved to straight section. Although this is not a wall-bounded flow, the results were used by the authors in the interpretation of curved turbulent boundary-layer data.

Maxey (1982) introduced the concept of an effective strain rate, α_{eff}, and showed that it is possible to write a transport equation for this quantity assuming homogeneous turbulence. Using the analogy with energy decay of homogeneous isotropic turbulence and introducing a large-eddy distortion time scale, $T_D = L/(\delta_D\sqrt{\overline{q^2}})$, where L is the integral length scale, δ_D is a constant and $\sqrt{\overline{q^2}}$ is the root-mean square (r.m.s.) of the trace of the Reynolds stress tensor, the following transport equation was obtained:

$$\frac{\partial \alpha_{eff}}{\partial t} = \frac{\partial \bar{U}}{\partial y} + \frac{\partial}{\partial y}\left(E_D\frac{\partial \alpha_{eff}}{\partial y}\right) - \frac{\alpha_{eff}}{T_D}. \tag{5}$$

This equation includes a diffusion term which accounts for the transport of effective strain by the advection of turbulent eddies, where E_D is the diffusion coefficient. However, this approach is applicable only in the case of single imposed strains or distortions, whereas in the case of a complex flow with multiple interacting strains, no formal theory yet exists. In addition, it is not clear how the different rates of application of a newly introduced strain rate affects the momentum transport inside a TBL.

The concept of total or combined effective strain rates has also been investigated in the past (cf. Maxey 1982; Sreenivasan 1985). Sreenivasan (1985) suggests that the turbulence structure at any given stage is completely determined by the local value of the total strain parameter

$$\beta_{TSt} = \int_0^{T_E} \left(\frac{\partial \bar{U}}{\partial y} \right) \mathrm{d}t, \tag{6}$$

if the applied mean shear is sufficiently large. Here, T_E is the typical lifetime of a large eddy (also eddy turnover time) which is of the order of $\frac{1}{3}\overline{q^2}/\varepsilon$, in equilibrium. Hence, the large-eddy lifetime can be viewed as the ratio of the turbulent kinetic energy to the isotropic turbulent dissipation rate. Note that this approach is strictly correct only for equilibrium flows. Sreenivasan (1985) also proposed that the non-uniqueness of the structural parameters for different experiments with similar β, for $\beta < 4$, suggests that $\mathrm{d}\beta/\mathrm{d}t$, i.e. its application rate, may be important in developing flows.

For the two-component data, an estimate for the total strain parameter can be found by expressing the large-eddy lifetime in terms of measured quantities, i.e.

$$\beta_{TSt,rad} \approx T_{E,rad} \frac{\partial \bar{U}}{\partial y} \approx \frac{1}{2} \frac{\overline{u^2} + \overline{v^2}}{-\overline{uv}} \frac{1}{1 - S_{rad}}, \tag{7}$$

respectively, where $S_{rad} = (\bar{U}/r)/(\partial \bar{U}/\partial y)$ is the curvature strain rate ratio. The total strain parameter can also be interpreted as the ratio of the large-eddy lifetime to a distortion time scale. This ratio is a useful measure to determine whether or not the flow should be treated as a rapidly distorted flow. In rapid distortion theory (RDT), the governing equations can be linearized under the assumptions that the turbulence is weak ($u' \ll U$) and that the distortion time is far less than a typical integral time scale, or in other words, $\beta_{TSt} \gg 1$ (see Savill 1987). Finally, it is important to note that the addition of a new strain will always have a greater effect on the turbulence structure than the continuous application of one to which the flow has already responded (Savill 1987). This is because the total effective strain experienced by a particular flow structure is limited by the large-eddy lifetime rather than the total applied strain.

The available information on complex flows with single or multiple interacting strain rates suggests that turbulence modelling using straightforward RANS will not be successful. For example the k–ε model is well known not to respond to mean flow rotation, and for similar reasons does not do well with curvature effects. Full Reynolds stress models do have terms that account for flow rotation; but the models for the fast pressure strain term typically do poorly for strong rotation, especially with added rates of strain (cf. the elliptical streamline work by Blaisdell & Shariff 1996). However, to be certain, we would have to do the calculations with the various models, including algebraic 1- and 2-equation models. It is expected that LES or DNS would be required to predict this flow accurately.

1.3. *Summary and objectives*

Despite a number of experimental studies on flows with multiple strain rates, there still is a lack of detailed, near-wall structural information concerning TBLs that experience controlled multiple pressure gradients. Few previous studies have addressed the mechanisms and degree to which multiple strain rates interact with each other within the turbulent boundary layer. Therefore, it is the primary objective of this investigation to study the response of a TBL to multiple extra rates-of-strain, i.e. radial and streamwise pressure gradients. Our brief review points to a number of unresolved issues requiring further consideration:

(i) Measure near-wall Reynolds stress data down to $y^+ = 10$ when multiple strains are applied.

(ii) Investigate to what extent the different strain rates interact with each other.

(iii) Investigate whether the boundary layer reaches a state of similarity and examine its equilibrium.

(iv) Investigate the response of the turbulent boundary layer immediately upstream and downstream of the onset of newly introduced strains (radial and streamwise).

(v) Investigate the response of bursting and the turbulence production cycle to multiple strain rates.

2. Experimental facility and techniques

2.1. *Water tunnel*

In order to investigate the influence of radial and streamwise strain rates on the turbulent flow field, it is crucial to provide a test environment in which the streamwise wall curvature and the streamwise variation of the cross-sectional area are carefully and accurately controllable. Figure 2 depicts the curved portion of the test section, showing the typical wall shapes used to establish the desired streamwise pressure distribution on the convex wall (the exact wall shapes are available in Schwarz 1998, tabulated wall shapes are also available at the *Journal of Fluid Mechanics* editorial office and at the web site http://widget.ecn.purdue.edu/∼tfpl/). Two test sections with different strengths of wall curvature were designed and manufactured to study the influence of streamline curvature and its interaction with streamwise pressure gradients.

All the data were acquired in a recirculating water channel facility (figure 3) driven by four centrifugal pumps each rated at $5.7 \times 10^{-3}\,\mathrm{m}^3\,\mathrm{s}^{-1}$ (90 g.p.m.). Two interchangeable curved test sections were employed to impose moderate and strong convex curvature. Softened and filtered water entered the straight development section through a series of screens, into a smooth two-dimensional contraction section followed by a honeycomb section to reduce large-scale vortical motions in the entrance region. An equilibrium turbulent boundary layer was developed on the smooth wall of the straight section (2.46 m long for test section 1, and 1.95 m long for test section 2). All test sections had a spanwise height of 200 mm (z-direction) and the width (y-direction) of the sections was 100 mm at the boundary-layer trip and approximately 110 mm at the entrance to the curved test section, $s = 0$. A flexible wall (constructed from 3.2 mm thick Lexan®) was placed between the measurement wall and the opposite sidewall to adjust the cross-sectional area, and hence to impose the streamwise pressure gradient. The flexible wall was adjusted to yield a zero pressure gradient (ZPG) in the straight portion and a ZPG, or adverse (APG) or favourable pressure gradients (FPG) of different strengths in the curved test section. The width

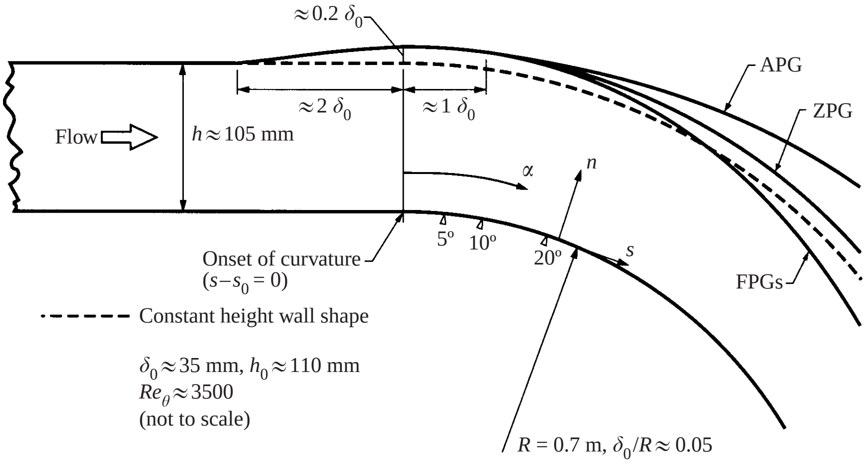

FIGURE 2. Diagram of curved test section and wall shapes.

of the test section downstream of the onset of curvature varied for each streamwise pressure gradient. A region of local acceleration persisted immediately downstream of the onset of curvature ($0 \leqslant s - s_0 \leqslant 2\delta_0$), owing to the discontinuity in wall curvature, despite widening of the cross-sectional area in that region. For additional details of the test section and pressure distribution see Schwarz (1998). For test section 1 (TS1), the boundary-layer thickness at the exit of the straight test section was $\delta_0 \approx 40$ mm, resulting in a curvature parameter of $\delta_0/R \approx 0.10$, which comprises a strong curvature. For test section 2 (TS2), the initial boundary-layer thickness was $\delta_0 \approx 35$ mm, which resulted in a curvature parameter of $\delta_0/R \approx 0.05$ (moderate curvature). Typical values of the curvature parameters under ZPG conditions for each test section were: $\Delta k^+ = 6.20 \times 10^{-5}$ for TS1 and $\Delta k^+ = 3.54 \times 10^{-5}$ TS2, using inner variables evaluated just upstream of the onset of curvature.

2.2. *Measurement techniques*

Pressure taps installed along the convex wall were used to measure the imposed streamwise pressure gradients with a Gilmont® micro-manometer. The manometer fluid used was carbon tetrachloride (CCl_4 with specific gravity = 1.584) allowing the pressure to be measured within 1 Pa. The pressure tap spacing was varied between 25.4 mm (near the onset of curvature) and 101.6 mm further downstream in the curved test sections.

A two-component laser-Doppler velocimeter (LDV) system was employed for simultaneous measurements of the streamwise and wall-normal instantaneous velocity. The transmitting optics of the two-component, three-beam LDV system consisted of a Thermo System Incorporated (TSI®) model 9100-8 velocimeter modified to measure velocity components at ±45° to the mean flow direction in TS1. A slightly different configuration was used for the velocity measurements in TS2, where the three-beam system was oriented to measure streamwise and wall-normal velocity components directly. Using a pair of Bragg cells, both monochromatic beams were frequency shifted at 40 MHz to minimize fringe biasing. Operating in the forward-scattering mode, near-wall measurements were made possible by inclining the optical axis of the transmitting side by approximately 3° with respect to the measurement wall. The probe volume was 45 μm in diameter and had a spanwise extent of approximately 920 μm, which corresponded to 2 and 40 viscous units, respectively, when normalized

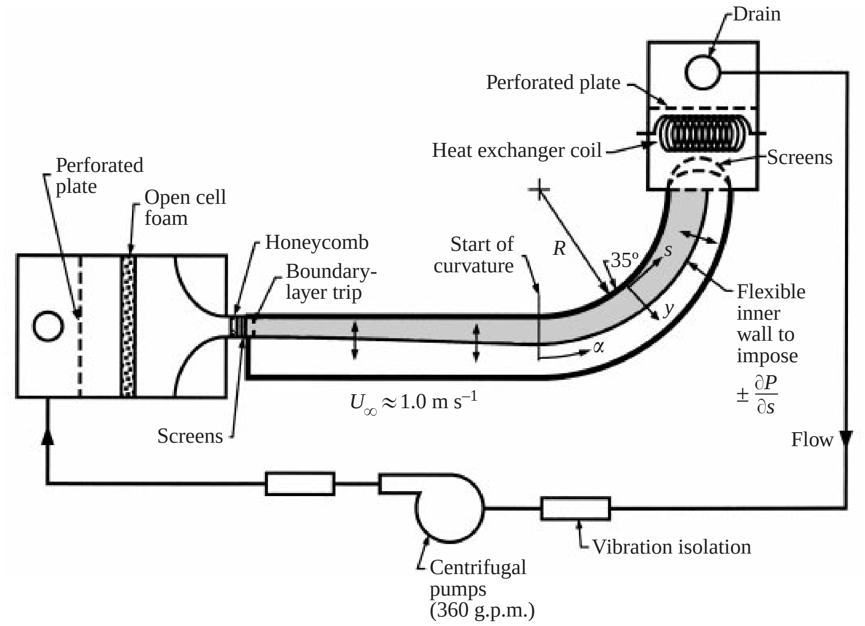

FIGURE 3. Diagram of low-speed water tunnel. TS1: $\delta_0/R = 0.10$; TS2: $\delta_0/R = 0.05$.

with inner variables, u_τ and ν. In order to enhance the spatial coincidence of the two probe volumes, a 50 μm pinhole was inserted into the receiving optics, which reduced the effective probe volume length to 12 viscous units. Spatial and temporal measurement coincidence were achieved by carefully aligning the transmitted beams and the receiving optics, and by setting a coincidence window on the counter processors (TSI 1980B) to ensure that the accepted signal on both channels originated from the same scattering particle passing through the probe volume (typical coincidence time was 30 μs). The flow was seeded with 0.3 μm diameter fat particles from homogenized cream at a concentration of approximately 2.5 ml m^{-3}.

In order to calculate reliable statistics (mean and higher-order moments), various numbers of statistically independent data realizations were required. For the two-component velocity profiles, a minimum of 10 000 data points were acquired for each velocity component. Velocity bias, which occurs in LDV measurements of turbulent flows (see McLaughlin & Tiederman 1973), was minimized using the fixed-waiting-time sampling method. Typical values for the inhibit time and validation rate (maintained at least five times in excess of the Kolmogorov frequency) were approximately 10–15 ms and 2500 Hz, respectively.

The time-resolved measurements, necessary for bursting period analysis, consisted of 100 000 velocity realizations with the counter processors operating in the single-point per Doppler-burst mode. In this case, velocity bias was reduced by correcting the individual velocity measurement using a two-dimensional weighting factor as suggested by McLaughlin & Tiederman (1973). During these measurements, the particle arrival rate was maintained in excess of the wall strain rate, which is an approximation for the viscous frequency of the flow, $f_{vis} = \partial \bar{U}/\partial y|_w = u_\tau^2/\nu$, which for TS1 was typically 1800 Hz for the zero, 2400–2800 Hz for the favourable, and 2700–650 Hz for the adverse streamwise pressure gradient cases. Note that for the APG case, the effects of convex curvature and pressure gradient oppose each other in terms of stabilizing or destabilizing the flow, resulting in a wide range of wall strain rates. For TS2, the typical values for the viscous frequency were 1600 Hz for ZPG, and 2900 Hz for the strong FPG case.

2.3. *Burst detection*

The structure of turbulence in boundary layers has been studied extensively (Robinson 1991). One of the events associated with coherent structures is an ejection, or series of ejections comprising a turbulent burst. The bursting cycle is the main turbulence production mechanism (Runstadler, Kline & Reynolds 1963). During an ejection event, the low-speed fluid near the wall undergoes a rapid acceleration away from the wall and mixes with the higher-speed fluid above the wall. Consequently, the ejection process is associated with a positive v-fluctuation (higher than the mean) and a negative u-fluctuation (lower than the mean). These characteristics led Lu & Willmarth (1973) to propose the second-quadrant (uv_2) burst-detection technique for an Eulerian velocity probe. This detector triggers on large negative values of the instantaneous product of the streamwise and wall-normal velocity fluctuations when they occur in the second quadrant of the uv-plane, i.e.

$$uv(t) < -Hu'v', \quad u(t) < 0 \quad \text{or } v(t) > 0, \tag{8}$$

where H is a threshold specified by the user. The fact that a threshold-independent range exists allows meaningful estimates of the mean time between bursts to be made. This detection method was chosen over single-component burst-detection methods, e.g. the VITA (Blackwelder & Kaplan 1976) and modified u-level (Bogard & Tiederman 1986) techniques, because the uv_2 method is known to give the best correlation between probe detections and visually observed ejections (Bogard 1982).

It was also necessary to group multiple ejections appropriately, depending on whether they originated from the same or from different bursts, through the use of a grouping time, τ_g. This grouping procedure was developed by Bogard & Tiederman (1986) and has also been used by other investigators (e.g. Barlow & Johnston 1988*b*; Schwarz & Plesniak 1996*a*). Ideally, a histogram of the time between ejections would have two separate distributions: one for ejections from the same burst and one for ejections from different bursts. In practice, there is some overlap between the two distributions. Ejections separated by τ less than τ_g are assumed to originate from the same burst, whereas those with longer separation times originate from different bursts. The appropriate grouping time for a given threshold can be determined using the histogram of the time between ejections plotted on a semi-logarithmic scale (see figure 4*a*). It is assumed that the distribution of times between ejections within the same burst and the time between detections from different bursts both decrease exponentially, yielding two linear regions with a region in between where the distributions overlap (not necessarily linear). The extrema of the overlap region are indicated by τ_1 and τ_2 and the grouping time was chosen at the midpoint of the overlap region (White & Tiederman 1990). Thus, the ambiguity in τ_g was half of the interval between τ_1 and τ_2. The propagation of this ambiguity is the major contributor to the uncertainty in the mean burst period $\bar{T}_B$. This grouping procedure was repeated for 10 different thresholds between 0.0 and 1.6 for each burst record. In figure 4(*b*), the burst period is plotted as a function of the detector threshold (H), and the threshold independent region is clearly evident. The reported time between bursts ($\bar{T}_B$) is calculated by simply averaging the values within the threshold independent range.

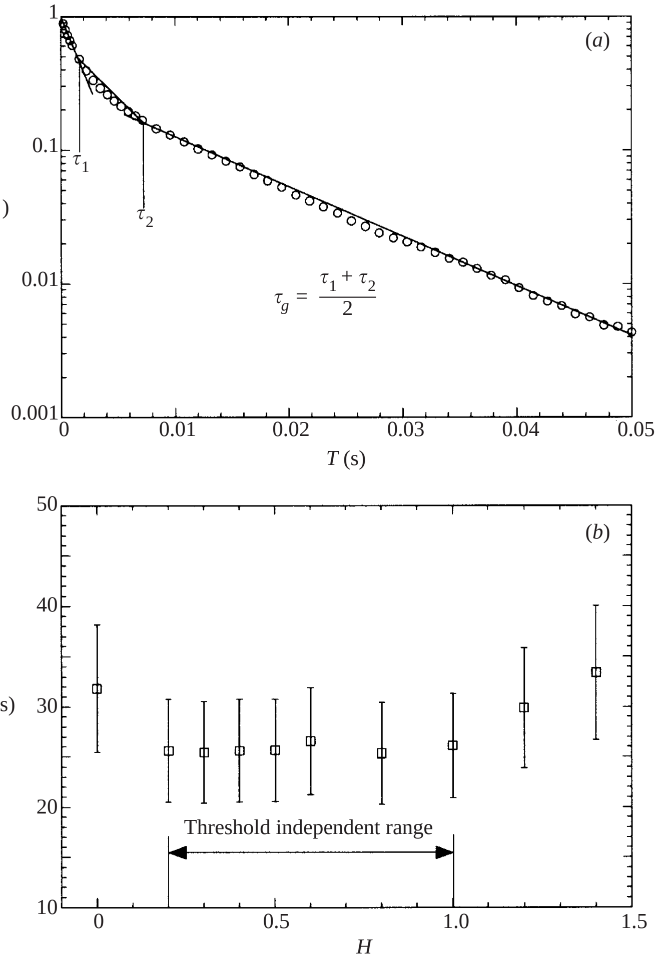

FIGURE 4. (*a*) Histogram of time between ejections to determine the grouping time. (*b*) Time between bursts as a function of detector threshold.

2.4. *Uncertainty estimates*

The error analysis for all measured quantities was based on the methodology outlined by Kline & McClintock (1953) and Moffat (1988). A 95% confidence interval for Gaussian (or nearly Gaussian) distributions was assumed. Calculation of uncertainty estimates for the LDV data followed the procedure used by Yanta & Smith (1973) and Walker & Tiederman (1988), and are reported in Schwarz (1998). The main source of error is the uncertainty in the determination of the beam-crossing angle, which affects the fringe-spacing calculation. This results in an uncertainty of 0.4% for the measured velocity component. In addition, the uncertainty in the estimate of statistical quantities depends on both the ensemble size and the r.m.s. level for a mean quantity, but solely on the ensemble size for a r.m.s. quantity.

Typical uncertainty bounds for the Reynolds stresses are shown in the upper right-hand corner of the appropriate figures. Typical uncertainties on the r.m.s. and mean velocities are of the order of the plot symbol sizes, i.e. less than 1%, except for the near-wall region ($y^+ \leqslant 10$, where $y^+ = yu_\tau/\nu$ is the inner normalized wall-normal

Quantity	$y^+ \approx 10$	$y^+ \approx 100$
$\sigma_{\bar{U}}$	±0.45%	±0.41%
$\sigma_{\bar{V}}$	±0.40%	±0.40%
$\sigma_{u'}$	±0.68%	±0.68%
$\sigma_{v'}$	±0.83%	±0.56%
$\sigma_{\overline{uv}}$	±7.15%	±5.26%

TABLE 1. Summary of measurement uncertainties for 95% confidence interval.

coordinate). For $y^+ \leqslant 10$, the measured wall-normal r.m.s. velocity component was significantly higher than the direct numerical simulation data by Spalart (1988) and hence is omitted. (Such an overprediction of the normal velocity fluctuations near the wall is common to many experimental data sets measured with LDV using various optics configurations (J. P. Johnston 1995 and R. L. Simpson 1996, personal communications) and is not fully understood.) The benchmark DNS results for the wall-normal r.m.s. velocity component exhibited the expected $O(y^2)$ behaviour. The maximum uncertainty on the shear stress was typically 12–13% in the maximum stress region ($y^+ \approx 40$–80). Typical values for the relative uncertainties for the mean and r.m.s. velocity components and for the primary Reynolds shear stress are given in table 1 for $N = 20\,000$ at $y^+ \approx 10$ and 100.

Uncertainty in the shear velocity is less than 1% due to the mean streamwise velocity measurements and approximately 5% due to the additional uncertainty introduced by the Clauser method, which has been used to infer the wall shear stress. Note that for flows with curvature and pressure gradient, the constants in the log-law may be different from the universal flat plate values (Moser & Moin 1987; Gibson 1988). The uncertainty for the pressure gradient parameter is of the same order as the size of the corresponding plotting symbols (1.6% for k).

The uncertainties associated with measuring quantities upon which the burst periods depend are of the order of 1–2%. However, owing to the post-processing operations, i.e. choice of thresholds, and determining grouping times to discriminate between ejections originating from the same or different bursts, the ambiguity in the absolute value of $\bar{T}_B$ is typically between 15 and 20%. Thus, although the absolute magnitudes of burst period are uncertain up to 20%, all of the data sets were processed consistently to minimize the ambiguity and the trends exhibited are faithful to within the measurement uncertainty of 2%. The normalized ejection duration $\Delta\tau_E^+ = \Delta\tau_E u_\tau^2/\nu$ was calculated from the individual time-resolved measurements for each threshold and its uncertainty is approximately ±3.5%.

3. Results and preliminary discussion

3.1. *Integral parameters and pressure gradients*

In figure 5, the distribution of the pressure gradient in terms of the acceleration parameter, $k = (\nu/U_e^2)(\mathrm{d}U_e/\mathrm{d}s)$, is shown for the moderate and strong curvature cases. All data sets are summarized in table 2. The ZPGU case is the ‘uncorrected’ zero pressure gradient in which the test section walls were parallel. Note the strong favourable pressure gradient which arises naturally at the straight/curved wall transition. This was counteracted in the ZPGC case by contouring the opposite wall. One objective of this study was to establish zero, as well as constant favourable and adverse

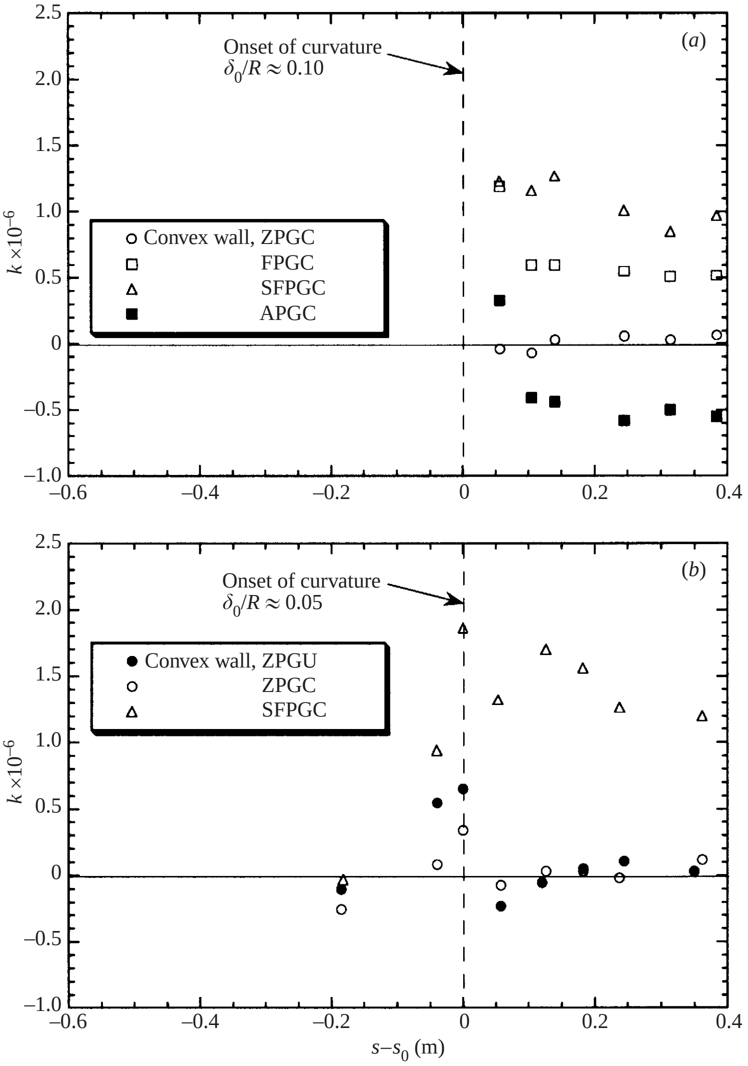

FIGURE 5. Acceleration parameter distributions along measurement wall for (*a*) strong and (*b*) moderate convex curvature (typical uncertainty on the order of plot symbol size).

pressure gradients of different magnitudes downstream of the onset of curvature. As shown in figure 5, nearly constant levels of pressure gradient were achieved over a significant portion of the convex wall ($\alpha > 10°$, corresponding to $s - s_0 \approx 1.7\delta_0$), except in the region immediately downstream of the onset of curvature, where a favourable pressure gradient (FPG) prevailed for a short distance. The flexible wall opposite to the measurement wall was carefully contoured to minimize this effect in the initial region of the curved test section. This was a painstakingly difficult iterative procedure that often took many hours because adjustments to the wall at one location change the pressure everywhere. Typical ranges for the acceleration parameter k, the momentum thickness Reynolds number Re_θ, and the pressure gradient ratio $P_{rat} = |\partial P/\partial s|/(\partial P/\partial r)$ were: $-0.5 \times 10^{-6} \leqslant k \leqslant 1.8 \times 10^{-6}$, $3500 \leqslant Re_\theta \leqslant 10\,500$, and $0 \leqslant P_{rat} \leqslant 31.2$, respectively.

Strong curvature ($\delta/R \approx 0.10$), TS1

Case	$k \times 10^6$	$\alpha = 8°$	15°	20°	35°	45°	55°
ZPGU	0.0	–	–	⊗	⊗	–	⊗
ZPGC	0.0	⊗	⊗	⊗	⊗	⊗	⊗
FPGC	0.5	⊗	⊗	⊗	⊗	⊗	⊗
SFPGC	1.0	⊗	⊗	⊗	⊗	⊗	⊗
APGC	−0.5	⊗	⊗	⊗	⊗	⊗	⊗

Moderate curvature ($\delta/R \approx 0.05$), TS2

Case	$k \times 10^6$	$\Delta s = -5\delta_0$	$-1\delta_0$	$\alpha = 0°$	5°	10°	15°	20°	30°
ZPGU	0.0	⊗	⊗	⊗	*	⊗	⊗	⊗	⊗
ZPGC	0.0	⊗	⊗	⊗	⊗	⊗	⊗	⊗	⊗
SFPGC	1.6	⊗	⊗	⊗	⊗	⊗	⊗	⊗	⊗

* no time-resolved data

TABLE 2. Summary of cases investigated
(⊗ indicates time-resolved, two-component velocity records).

z [mm]	$c_f \times 10^3$	δ^* [mm]	U_{pw} [m s^{-1}]
−40	2.348	5.08	1.189
−20	2.350	4.81	1.218
0	2.438	4.46	1.214
20	2.551	4.41	1.195
40	2.444	4.98	1.188

TABLE 3. Spanwise (z-direction) variation of integral parameters at $\alpha \approx 35°$ under ZPG conditions

Spanwise variations of integral parameters were evaluated from single-component LDV measurements to check the mean two-dimensionality of the flow. Representative values of the skin-friction, displacement thickness, and potential wall velocity at five spanwise locations are given in table 3. The flow is reasonably two-dimensional at this streamwise location ($\alpha \approx 35°$), where the largest variation of $\pm 5.1\%$ occurred for the skin-friction coefficient. Flow visualization by Richman (1994) did not reveal any strong secondary flows over the central 50% of the span. Furthermore, the correlation coefficient was well behaved and showed no evidence of boundary-layer contamination, even for the APG cases with the thickest boundary layer (Schwarz 1998).

The distribution of the local skin-friction coefficient in each test section is shown in figure 6. Despite the positive shift near the onset of curvature for both test sections (owing to the locally strong FPG), the skin-friction coefficient is reduced over the convex wall in the presence of zero pressure gradient (ZPG) in both test sections. The degree of reduction is greater for the stronger curvature, as expected. On the other hand, different levels of FPG counteract the reduction caused by the convex curvature, whereas adverse pressure gradient (APG) augments the reduction of the skin-friction over the convex wall for TS1. This behaviour is a clear indication for an interactive process taking place between the two applied extra rates-of-strain. The same circumstances were observed in the skin-friction distribution measured by Bandyopadhyay & Ahmed (1993), where the S-shaped duct resulted in asymmetrical responses between the two walls, clearly implying the interaction of the radial and streamwise strain rate.

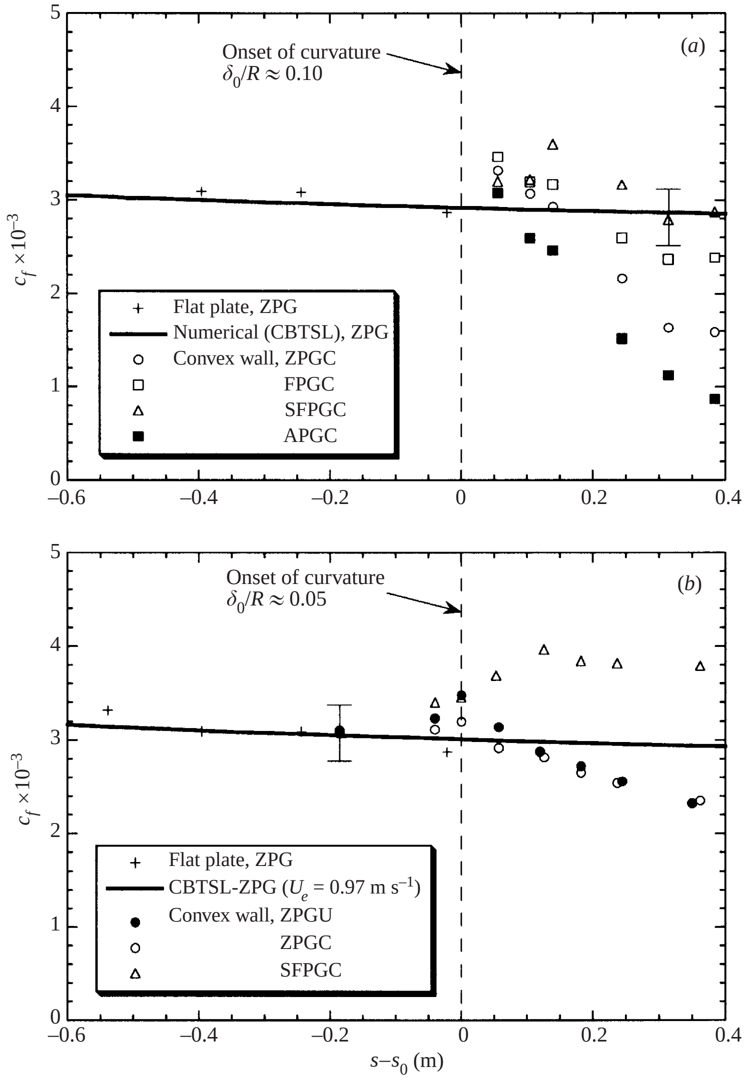

FIGURE 6. Distributions of skin-friction coefficient along measurement wall for (*a*) strong and (*b*) moderate convex curvature.

3.2. *Strong curvature case*

A strong curvature case is considered first ($\delta_0/R \approx 0.10$, where δ_0 is the initial boundary-layer thickness upstream of the onset of curvature and R is the radius of curvature). Two-component velocity profiles were acquired at different streamwise locations along the convex wall in the mid-plane of the test section ($z = 0\,\text{mm}$) as the flow was exposed to zero, two different favourable and one adverse streamwise pressure gradient. The pressure gradient ratio, P_{rat}, in this test section was varied between 0 for the ZPG and 0.6 for the SFPG case. Mean and higher-order velocity statistics are presented below to illustrate the downstream development of the TBL under ZPG conditions and to show the effect of different streamwise pressure gradients at one fixed streamwise location ($\alpha \approx 35°$) on the turbulence structure of the boundary layer. All data sets are compared to a ZPG boundary layer over a smooth flat wall

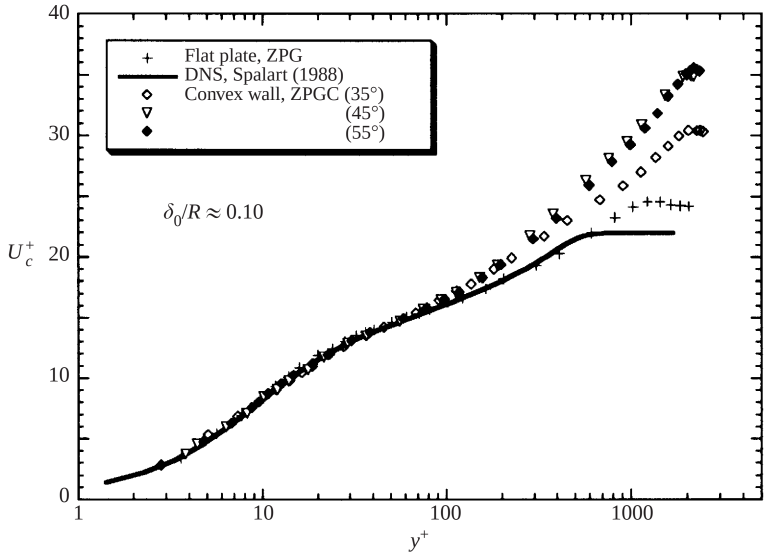

FIGURE 7. Mean streamwise velocity profiles for TS1 under compensated zero pressure gradient conditions (ZPGC) (typical uncertainty of the order of plot symbol size).

with $Re_\theta \approx 3250$ and to the DNS results of Spalart (1988), where $Re_\theta = 1410$. The shear velocity, u_τ, has been used for inner variable normalization. It was determined using the standard Clauser method, although the log-law must be used cautiously in curved TBLs (cf. Gibson 1988; Schwarz & Plesniak 1996*b*). In this study, the classical constants ($\kappa = 0.41$ and $B = 5.0$) were retained to evaluate the shear velocity, primarily because no direct measurements of the wall shear stress were available and to facilitate comparison to the vast body of previous work on curved boundary layers (cf. So & Mellor 1973; Smits *et al.* 1979; Gillis & Johnston 1983; Muck *et al.* 1985; Barlow & Johnston 1988*a, b*).

In figures 7 and 8, the streamwise development of the mean and fluctuating velocity and Reynolds shear stress profiles over a strongly curved convex wall with zero streamwise pressure gradient (ZPG) is shown. As previously reported (e.g. Gillis & Johnston 1983; Gibson, Verriopoulos & Vlachos 1984), the extent of the logarithmic region is reduced ($30 \leqslant y^+ \leqslant 100$) owing to the presence of the strong convex curvature. An explicit relationship for the mean streamwise velocity component as suggested by Liakopolous (1984) represents the near-wall behaviour throughout the logarithmic region very well (not plotted), as did the DNS results of Spalart (1988) (plotted with solid line). Initially, the wake component in the outer portion of the turbulent boundary layer increases with downstream distance up to $\alpha \approx 45°$. It then remains constant, implying mean flow similarity. Note that the deviation of the current flat-plate data from the DNS results in the outer portion of the boundary layer is due to the different Reynolds numbers of each of these studies.

Similarity for the Reynolds stresses is also achieved by 45°. The normal components of the Reynolds stress (streamwise and wall-normal r.m.s. velocities), shown in figures 8(*a*) and 8(*b*), collapse throughout the entire boundary layer at every streamwise location. The primary peak in the streamwise r.m.s. velocity occurred at the same wall-normal distance ($y^+ \approx 15$) as for the flat plate case. However, the peak values were approximately 14% lower than those measured on the flat plate. The increase of both components relative to the flat plate values in the outer portion of the TBL is attributable to a difference in Reynolds number and to boundary-layer contamination (especially at the last two measurement stations).

In figure 8(*c*), the primary Reynolds shear stress profiles again exhibit similarity over the curved wall. There is a dramatic reduction in the primary Reynolds shear stress outside the logarithmic region with respect to flat-plate values, which has been reported by other investigators (e.g. So & Mellor 1973; Gillis & Johnston 1983) and can be attributed to the attenuation of the larger-scale structures in the outer portion of the boundary layer owing to the strong stabilizing convex curvature, as observed by Chiwanga & Ramaprian (1993). They showed that the size of the energy-containing eddies was reduced dramatically for a flow over a convex surface even with moderate curvature (their curvature parameter was $\delta_0/R \approx 0.04$). The eddies are smaller because the streamlines near the free stream have a convex curvature and the resulting normal pressure gradient causes a reduction in the entrainment of the ambient fluid by the boundary layer.

In figure 9, the mean streamwise velocity profile is shown as a function of the normalized wall-normal coordinate with zero, favourable and adverse streamwise pressure gradient at a fixed streamwise location ($\alpha \approx 15^\circ$). This particular streamwise distance was chosen because it is far enough downstream of the region that is influenced by a locally strong FPG which arises because of a sudden change in wall curvature from an infinite radius of curvature (flat plate) to a finite radius. The mean profiles collapse well throughout the logarithmic region, whereas the wake component (outer portion of the turbulent boundary layer) is reduced with increasing strength of FPG, and elevated for APG. Favourable pressure gradient has the tendency to oppose the wake-enhancing effect of the convex curvature, whereas the APG further increases the wake component. On the other hand, both convex curvature and FPG tend to stabilize the turbulence within the boundary layer, whereas APG acts to destabilize it.

The streamwise and normal r.m.s. velocities, along with the primary Reynolds shear stress (shown in figure 10) are illustrative of the effects of the imposed extra rates of strain. The near-wall values ($y^+ \leqslant 50$) of the normal stresses collapse for all cases except for the APG case. Changes are compensated by changes in u_τ when subjected to multiple strain rates of different magnitude. Hence, inner scaling is successful in the inner region of the boundary layer when favourable pressure gradients are applied along with convex curvature. The reduction of the primary peak in the streamwise r.m.s. velocity relative to the measured flat-plate values occurs in all cases, even in the presence of APG. Beyond the near-wall region, all Reynolds stress components for the ZPG and FPG cases are reduced relative to the flat-plate values, except in the wake region. This reduction was augmented by the FPGs and counteracted by the APG. Similar effects have been observed in flat-plate turbulent boundary layers subjected to streamwise pressure gradients (Koskie 1991; Smits, Matheson & Joubert 1983). Note that the wall-normal r.m.s. velocity component remains elevated, relative to the flat-plate values, throughout the entire boundary layer in the presence of APG and that the streamwise r.m.s. component is elevated just outside the inner region of the TBL ($y^+ > 30$). The primary Reynolds shear stress, shown in figure 10(*c*), exhibits noteworthy features as well. Beyond the shortened logarithmic region, $-\overline{uv}/u_\tau^2$ is reduced relative to the flat-plate values. This is attributable to the attenuation of the larger-scale structures in the outer portion of the boundary layer, as discussed previously. The additional effect of the various streamwise pressure gradients on the primary Reynolds shear stress is noticeable throughout almost the entire boundary layer. In general, the FPGs tend to reduce the turbulent shear stress correlation,

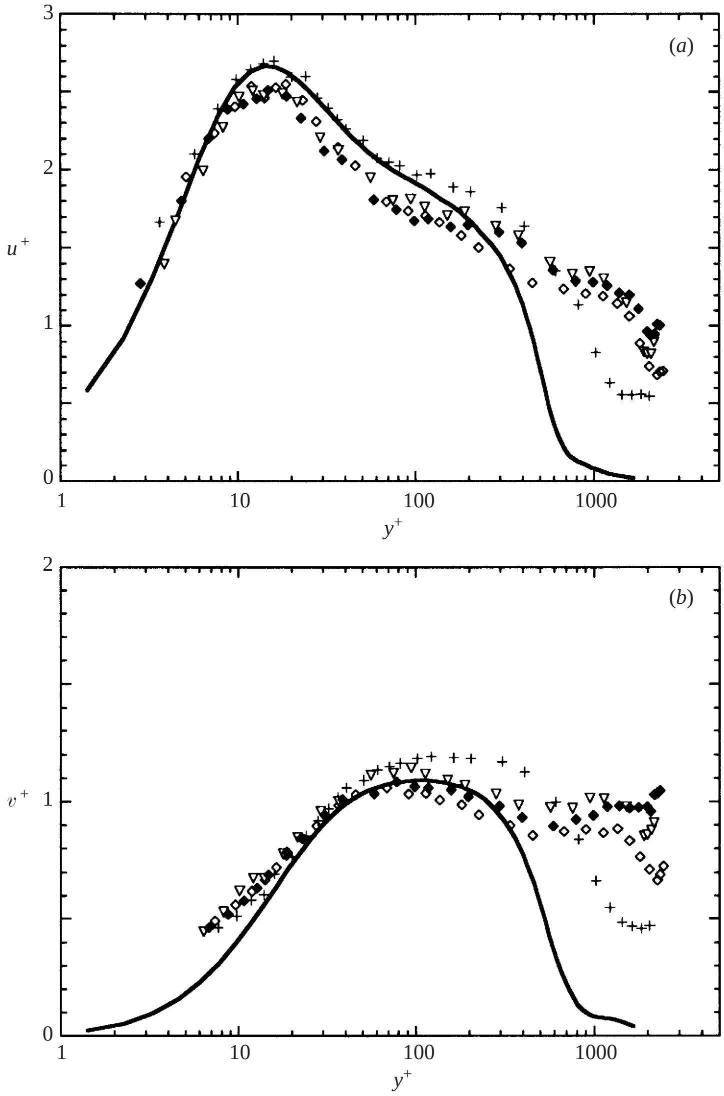

FIGURE 8(*a*, *b*). For caption see facing page.

whereas the APG has the opposite effect. Based on comparisons within the maximum shear stress region of each additional streamwise strain with the ZPG case, FPG caused a reduction by 7% and SFPG a reduction by 25%. On the other hand, the maximum value for the Reynolds shear stress was increased by 40% in the presence of APG.

3.3. *Moderate curvature case*

In this section, mean and higher-order velocity statistics are presented for the test section with moderate curvature ($\delta_0/R \approx 0.05$ and $0 \leqslant P_{rat} \leqslant 1.2$) to illustrate the behaviour of the TBL immediately upstream and downstream of the onset of curvature under ZPG and SFPG conditions. As in § 3.2, all data sets are normalized using u_τ and compared to a ZPG flat-plate boundary layer with $Re_\theta \approx 3250$ and to the DNS results of Spalart (1988).

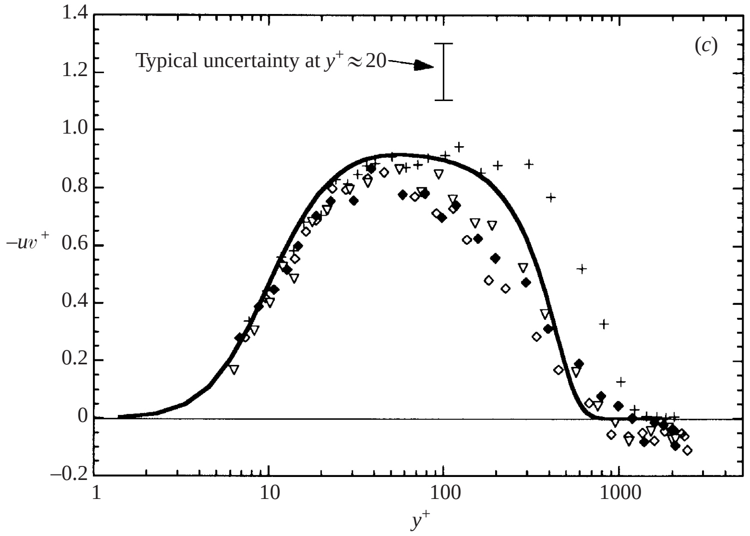

FIGURE 8. Profiles of (*a*) streamwise and (*b*) wall-normal r.m.s. velocity (typical uncertainty on the order of plot symbol size); and (*c*) primary Reynolds shear stress profiles for TS1 under compensated zero pressure gradient conditions (ZPGC). $\delta_0/R \approx 0.10$. See figure 7 for key.

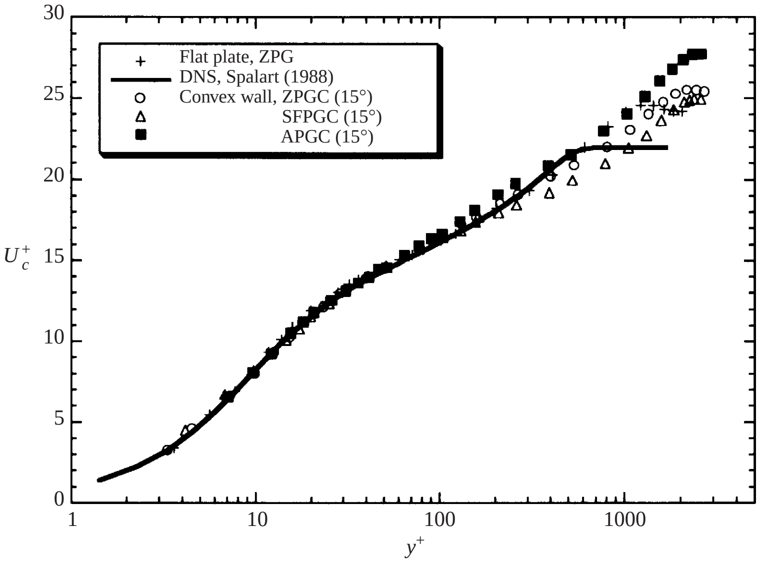

FIGURE 9. Mean streamwise velocity profiles for TS1 under different streamwise pressure gradient conditions at $\alpha \approx 15°$ (uncertainty of the order of plot symbol size). $\delta_0/R \approx 0.10$.

The mean streamwise velocity profiles shown in figure 11 for ZPG at different streamwise locations, starting 5 boundary-layer thicknesses upstream of the onset of curvature and extending 10° downstream, collapse very well. It is virtually impossible to distinguish between flat-plate data and the data that were acquired in the curved test section. Even at the last streamwise location ($\alpha \approx 10°$), the extent of the log-law region has not been reduced by the action of the convex curvature. Any changes in the strength of the wake component are minimal.

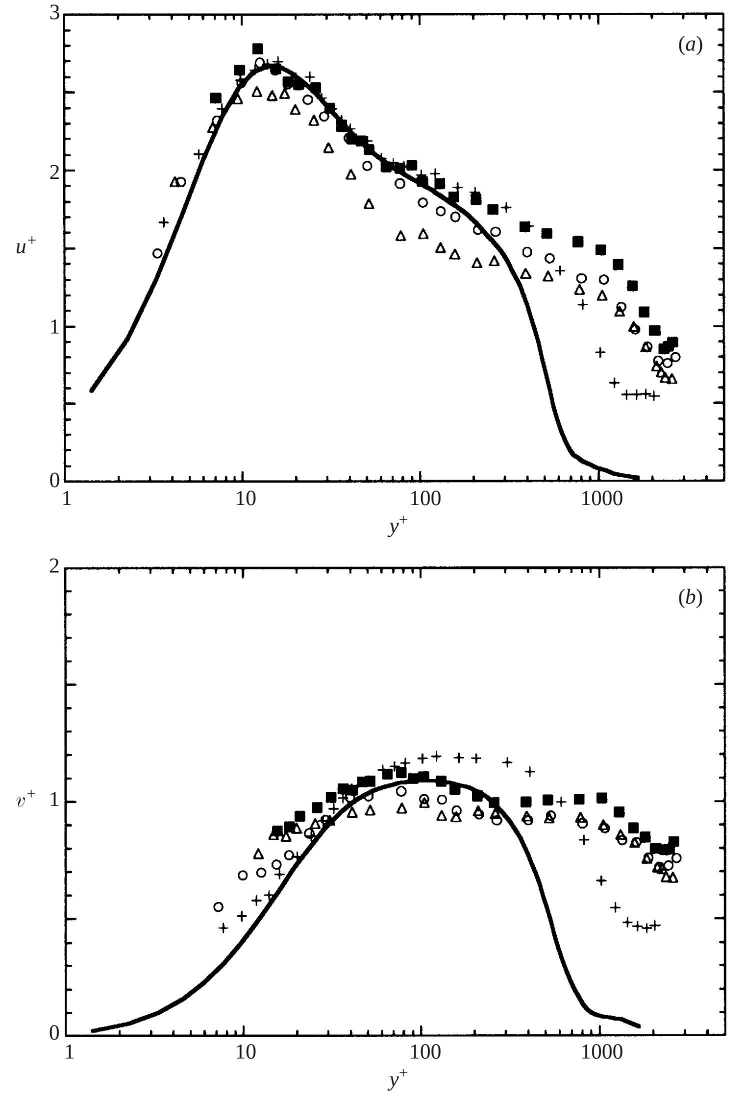

FIGURE 10(*a*, *b*). For caption see facing page.

Despite the lack of differences in the mean streamwise velocity profiles, there are some noteworthy variations in the Reynolds stress profiles shown in figure 12. The fluctuating velocity profiles clearly show a monotonic reduction of both the streamwise and wall-normal r.m.s. velocities immediately at the onset of curvature ($\alpha \approx 0°$). Profiles of the primary Reynolds shear stress, shown in figure 12(*c*), exhibit even more significant differences between the turbulence upstream and downstream of the onset of curvature. Beginning at $\alpha \approx 0°$, the peak in $-uv^+$ is reduced relative to the upstream stations, and this trend continues as the flow develops along the convex wall. The most significant reduction can be observed outside the near-wall region ($y^+ > 70$). This behaviour clearly shows that the convex curvature immediately reduces the turbulent momentum transport in the TBL, yet the mean streamwise velocity profiles remain unaltered.

In figures 13 and 14, the mean and fluctuating velocity profiles as well as profiles

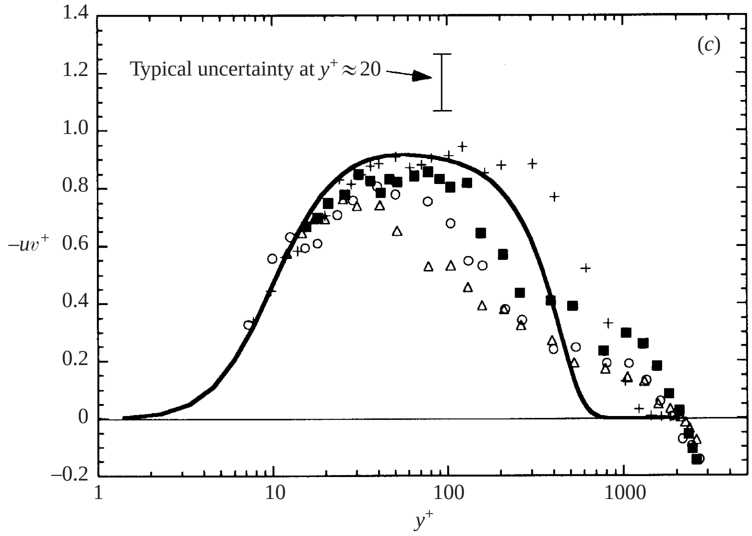

FIGURE 10. Profiles of (*a*) streamwise and (*b*) wall-normal r.m.s. velocity (typical uncertainty on the order of plot symbol size); and (*c*) primary Reynolds shear stress profiles for TS1 under different streamwise pressure gradient conditions at $\alpha \approx 15°$. $\delta_0/R \approx 0.10$. See figure 9 for key.

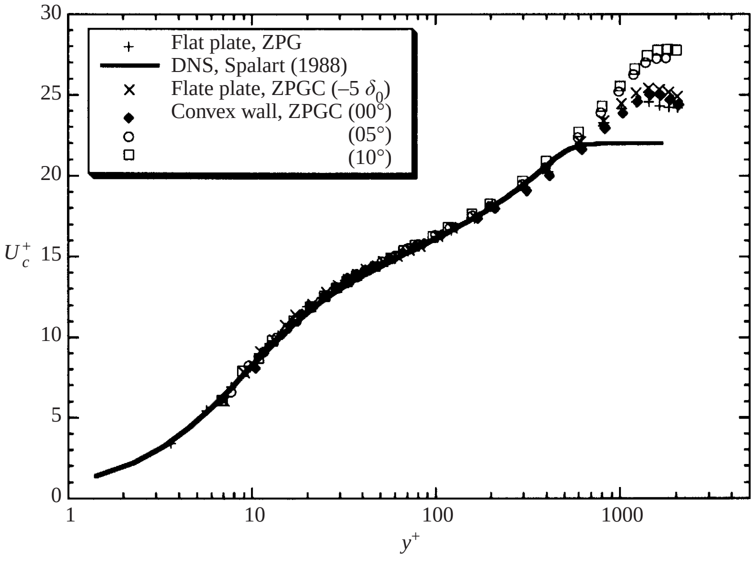

FIGURE 11. Mean streamwise velocity profiles for TS2 under zero pressure gradient conditions ZPGC (typical uncertainty of the order of plot symbol size). $\delta_0/R \approx 0.05$.

of the primary Reynolds shear stress are shown for the same streamwise locations as above under SFPG conditions. Some remarkable differences (compared to the ZPG case) can be observed. The wake component of the mean streamwise velocity profile is suppressed even upstream of the onset of curvature. In contrast to the ZPG data, these profiles collapse only throughout the log-law region of the boundary layer, but deviate in the outer layer.

The effect of the applied SFPG on the fluctuating velocity components is similar

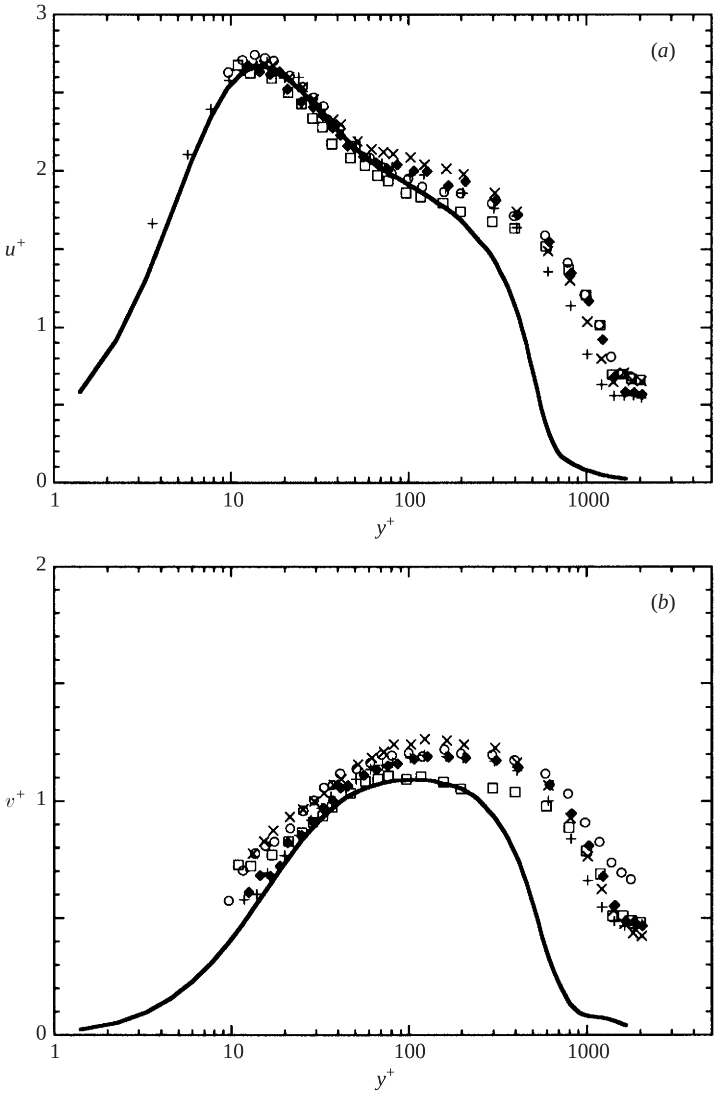

FIGURE 12(a, b). For caption see facing page.

to that found in the presence of ZPG, as shown in figures 14(a) and 14(b). The monotonic reduction of both the streamwise and the wall-normal r.m.s. velocity is more dramatic than before and can be observed to begin upstream of the onset of curvature. This effect is solely caused by the application of a favourable pressure gradient. However, it is the onset of curvature itself, combined with the reduction of the cross-sectional flow area at the onset of curvature that impose the favourable pressure gradient. The reduction of the primary Reynolds shear stress immediately downstream of the onset of curvature (figure 14c) is also more pronounced than in the ZPG case. Note that in the presence of SFPG, the reduction of $-uv^+$ occurs throughout almost the entire boundary layer ($y^+ \geqslant 15$). This striking behaviour indicates that the largest portion of the turbulent boundary layer is affected when a strong FPG is applied in combination with moderate convex curvature. Note that the

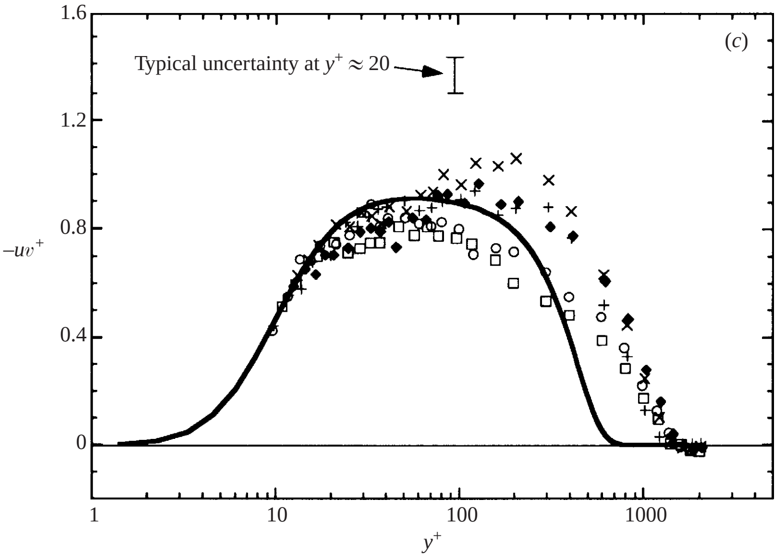

FIGURE 12. Profiles of (*a*) streamwise and (*b*) wall-normal r.m.s. velocity (typical uncertainty on the order of plot symbol size); and (*c*) primary Reynolds shear stress profiles for TS2 under zero pressure gradient conditions (ZPGC). $\delta_0/R \approx 0.05$. See figure 11 for key.

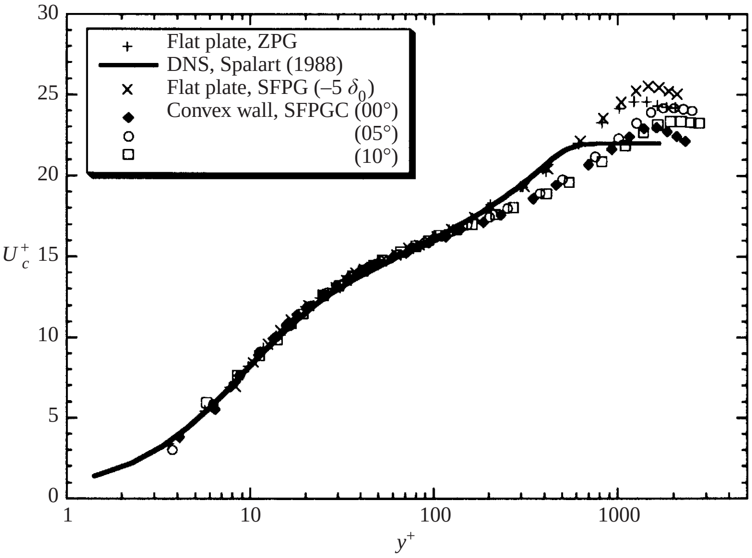

FIGURE 13. Mean streamwise velocity profiles for TS2 under strong favourable pressure gradient conditions SFPGC (typical uncertainty of the order of plot symbol size). $\delta_0/R \approx 0.05$.

pressure gradient ratio in this case is twice as large as that for the strong curvature case combined with SFPG.

These results clearly demonstrate that the turbulence is immediately affected by the imposed extra strain rates, i.e. radial and streamwise pressure gradients. Even in the absence of the strong favourable pressure gradient, the measured Reynolds normal and shear stresses were reduced at the start of curvature. This trend was amplified as an SFPG was imposed along with convex curvature. This behaviour is

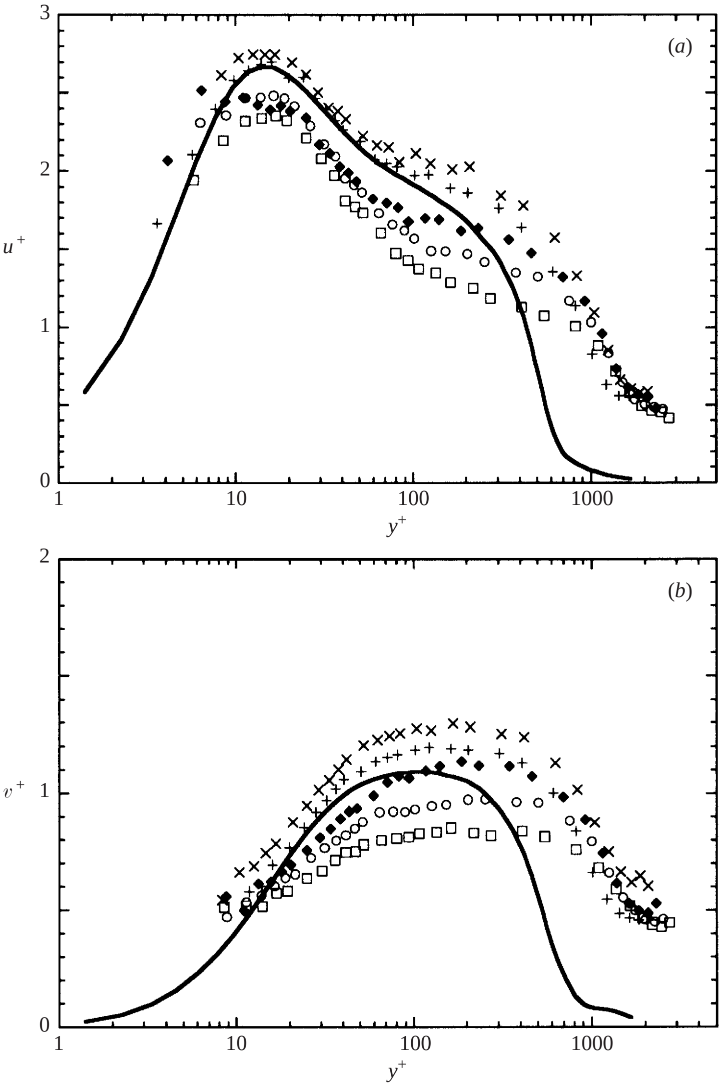

FIGURE 14(a, b). For caption see facing page.

not unexpected, since both extra strain rates tend to stabilize the turbulence within the boundary layer.

4. Further discussion

In this section, we will first examine whether the boundary layer reaches a new state of equilibrium some distance after the extra strain rates are introduced. This is an important consideration, since common turbulence models (e.g. k–ε two-equation model) require local equilibrium conditions. In the following subsections, the effect of different values of the pressure gradient ratio, $P_{rat} = (\partial P/\partial s)/(\partial P/\partial n)$ on the turbulence will be investigated. Representative production terms of the Reynolds stress tensor, as well as profiles of the flux Richardson number, are presented. Finally,

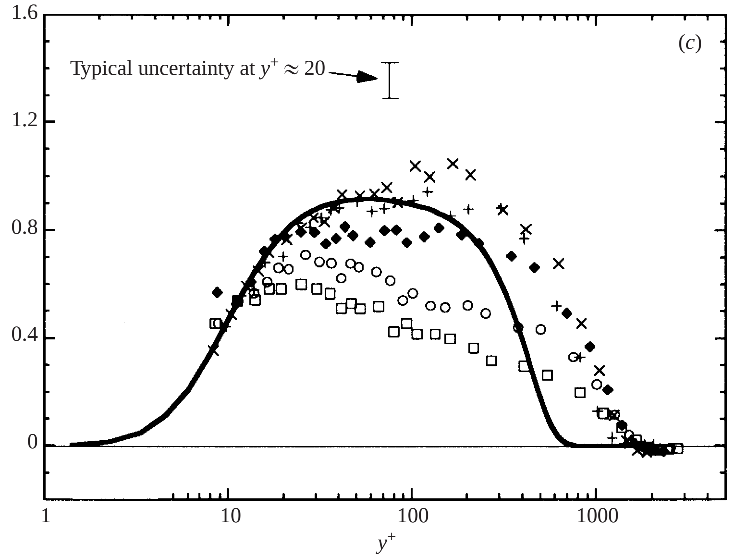

FIGURE 14. Profiles of (*a*) streamwise and (*b*) wall-normal r.m.s. velocity (typical uncertainty of the order of plot symbol size); and (*c*) primary Reynolds shear stress profiles for TS2 under strong favourable pressure gradient conditions (SFPGC). $\delta_0/R \approx 0.05$. See figure 13 for key.

the response of the turbulence production cycle (and bursting) to multiple strain rates will be discussed.

4.1. *Examination of equilibrium*

A turbulent boundary layer becomes an equilibrium layer when the velocity profiles are independent of the Reynolds number and the downstream distance s, if non-dimensionalized using an appropriate velocity-defect law (Tennekes & Lumley 1972). Strictly speaking, a given class of shear flows achieves some state of dynamical equilibrium, in which the local energy input should approximately balance the local loss (mostly through viscous dissipation), i.e.

$$-\overline{uv}\frac{\partial \bar{U}}{\partial y} + \varepsilon \approx 0. \tag{9}$$

Equation (9) governs the transport of turbulent kinetic energy for homogeneous, stationary turbulence (Hinze 1975).

The most common thickness parameter for equilibrium flows (White 1974) was determined by Clauser and is defined as:

$$\Delta = \int_0^\infty \frac{U_e - \bar{U}}{u_\tau}\,\mathrm{d}y = \delta^* \lambda, \tag{10}$$

where $\lambda = \sqrt{2/c_f}$. All velocity profiles can be scaled with y/Δ for constant Clauser equilibrium shape factor given by:

$$G = \frac{1}{\Delta}\int_0^\infty \left(\frac{U_e - \bar{U}}{u_\tau}\right)^2 \mathrm{d}y. \tag{11}$$

The departure and return to equilibrium can be described in the (G, β)-plane, where

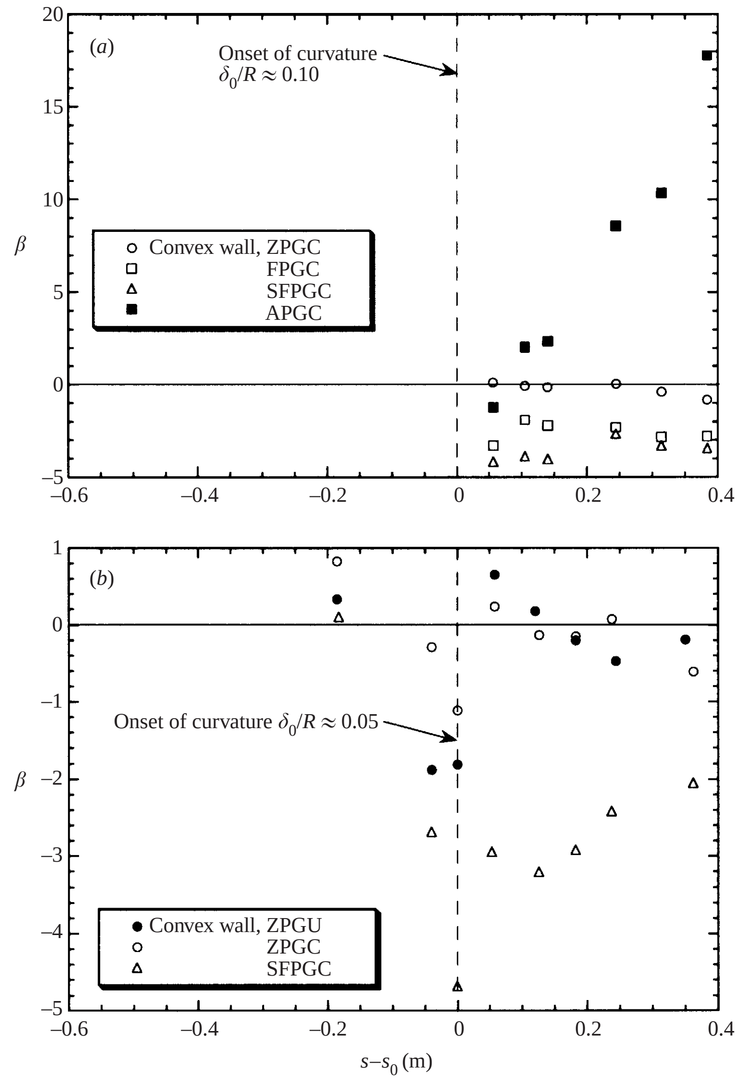

FIGURE 15. Clauser equilibrium parameter for (*a*) strong and (*b*) moderate convex curvature (uncertainty of the order of plot symbol size).

β is the ratio of pressure to wall friction forces given by

$$\beta = \left(\frac{\delta^*}{\tau_w}\right)\left(\frac{\mathrm{d}P}{\mathrm{d}s}\right). \tag{12}$$

The (G, β)-plane shows the response of the boundary-layer physics as reflected through the integral measure of equilibrium (G) to an applied strain rate, or input to the boundary-layer physics, measured via β. It is expected that the response is not necessarily instantaneous, but rather that there is a lag to the imposed strain rate, or perhaps a lead as found in three-dimensional turbulent boundary layers near separation. This is examined in terms of the relative change of angles of the principal axes or strain rate and Reynolds shear stress in § 4.5.

Before examining the behaviour in the (G, β)-plane, the streamwise development

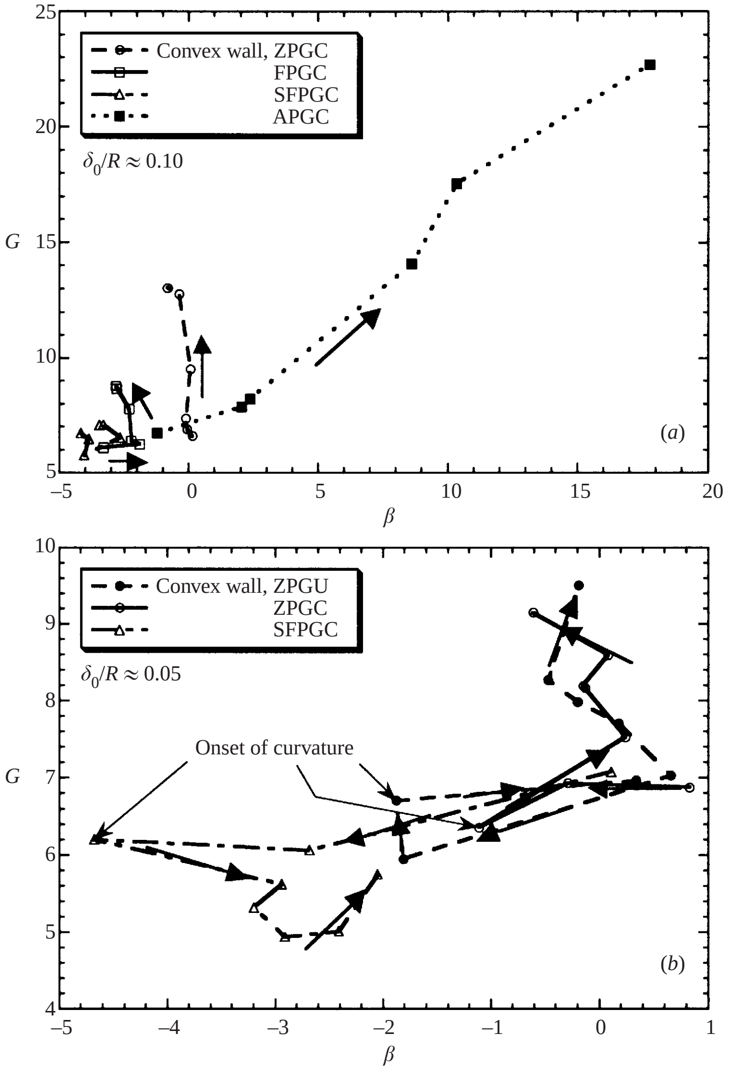

FIGURE 16. Pressure gradient trajectories for (*a*) strong and (*b*) moderate convex curvature (uncertainty of the order of plot symbol size). Arrows indicate direction of increasing streamwise distance.

of the Clauser equilibrium parameter is shown in figure 15. It is obvious that the TBL subjected to the adverse pressure gradient combined with the strong curvature never reaches equilibrium. On the other hand, β tends to constant values as the flow develops along the convex wall for all other cases indicating that the boundary layer might reach a new state of local equilibrium, a criterion that must be satisfied to employ certain turbulence models.

In figure 16, the (G, β) trajectories are shown for the different streamwise pressure gradients in both test sections. For the strong curvature case, shown in figure 16(*a*), it is clear that the trajectories for ZPG and APG move away from the initial equilibrium, an effect that is more pronounced for the APG case. The initial measuring station in all cases except ZPGC has the lowest value of β, so the trajectories begin at the leftmost point on the trajectory curve and proceed in the direction indicated by

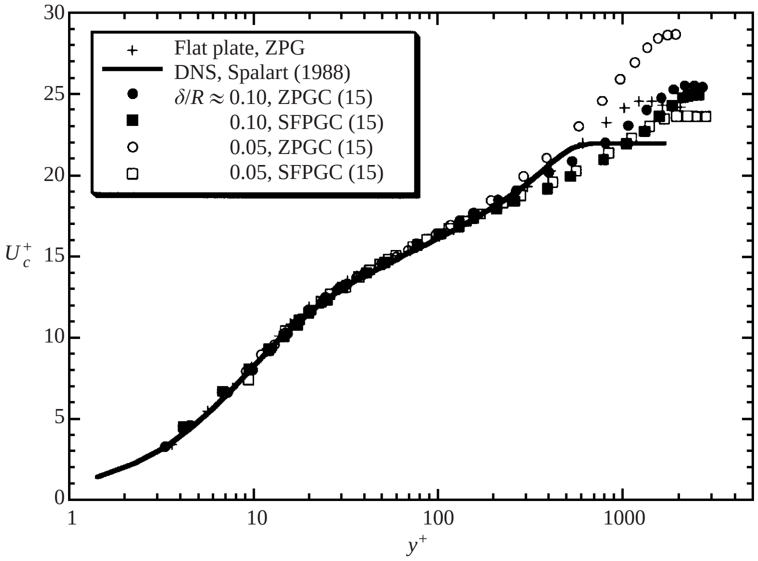

Figure 17. Mean streamwise velocity profiles for TS1 and TS2 under different streamwise pressure gradient conditions at $\alpha \approx 15°$ (uncertainty of the order of plot symbol size).

the arrows. In the presence of ZPG and SFPG, the boundary layer reaches a new equilibrium condition (with $G \approx 12.9$ for ZPG and $G \approx 7.1$ for SFPG). Note that the symbols for the last two measuring stations overlap for these two cases.

It is perhaps surprising that for moderate curvature (TS2, figure 16*b*), G is rather far from the initial equilibrium at the last measurement location ($\alpha \approx 30°$) for both ZPG cases, whereas in the presence of SFPG, the trajectory tends to return to the initial equilibrium condition, in a nonlinear fashion. All of these cases begin their trajectory with slightly positive values of β and proceed in the direction indicated by the arrows. The same trend of return to equilibrium for the SFPG case can be observed for TS1. Similar behaviour was reported by Bandyopadhyay & Ahmed (1993) on both walls of an S-shaped duct. They pointed out that in the flat recovery section downstream of curvature, the equilibrium values for G measured in the upstream flat section were not achieved and termed this effect a hysteresis of the large eddies. They also emphasized the importance not only of β, but also the effect of $\mathrm{d}\beta/\mathrm{d}s$ when modelling turbulent boundary layers with streamwise pressure gradient. Note that $\mathrm{d}\beta/\mathrm{d}s$ accounts for the application rate of the streamwise pressure gradient.

4.2. *Multiple strain rate ratios*

In order to illustrate the effect of different ratios of strain rates (radial to streamwise), profiles of the mean streamwise velocity and the Reynolds stress components are compared for different strengths of curvature ($\delta_0/R \approx 0.05$ and $\delta_0/R \approx 0.10$) combined with zero and strong favourable pressure gradients. These profiles are shown for one fixed streamwise location ($\alpha \approx 15°$) in figures 17 and 18. The pressure gradient ratio, $P_{rat} = (\partial P/\partial s)/(\partial P/\partial n)$, ranges from 0 to 1.2. It should be noted that the asymptotic limit $\partial P/\partial n \rightarrow 0$ which causes P_{rat} to become infinite is not physically meaningful because the absence of curvature constitutes an entirely different flowfield, and the usefulness of forming the ratio is unclear. The inner-normalized curvature parameters ($\Delta k^+ = \Delta R\nu/u_\tau$) were 6.20×10^{-5} for TS1 and 3.54×10^{-5} for TS2, respectively.

Another measure of the relative importance of curvature and streamwise pressure

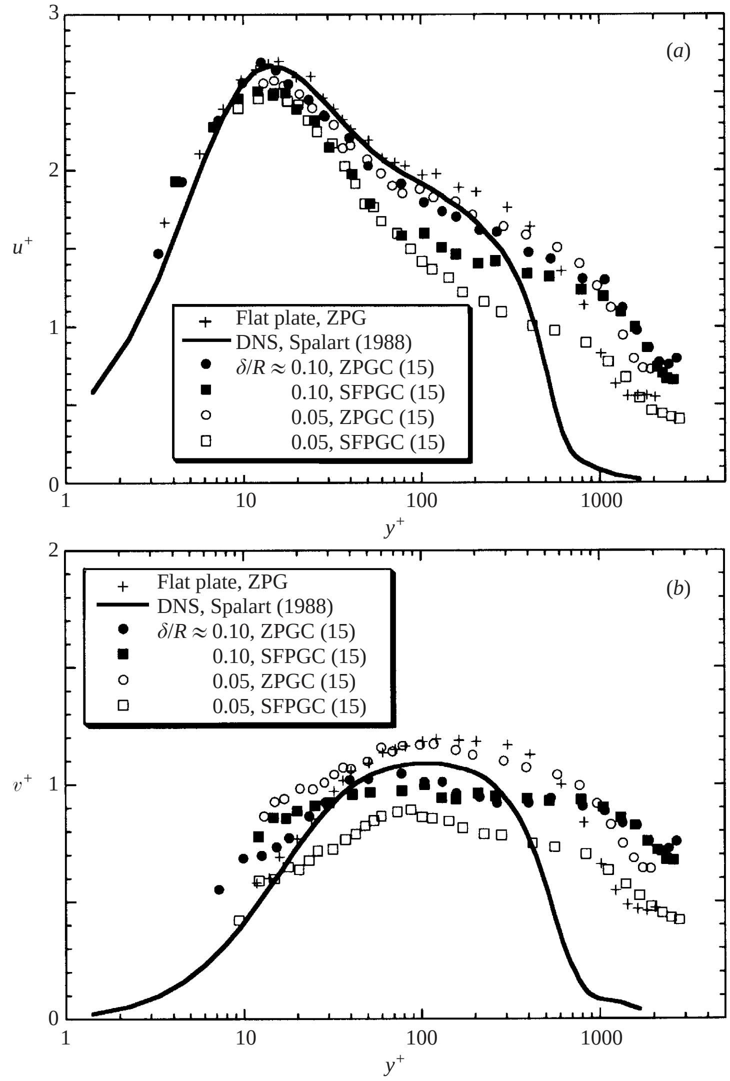

FIGURE 18(*a*, *b*). For caption see facing page.

gradient effects is the ratio of 'normal stress production' and mean shear production (Chebbi *et al.* 1998). The mean shear production is usually affected by curvature (through its effect on uv) more than the direct production by the extra strain rate due to curvature, U/R. This parameter is defined below:

$$F = \frac{-(\overline{u^2} - \overline{v^2})\,\partial U/\partial s}{-\overline{uv}\,\partial U/\partial y}. \tag{13}$$

In the present experiments, typical magnitudes for this ratio for both ZPG cases range from 2 to 3×10^{-6} in the near-wall region to 3 to 4×10^{-5} in the outer portion of the TBL. Note that the values are non-zero owing to a slight non-zero pressure gradient in the test section. On the other hand, for the SFPG cases, the ratio varies from 1 to 2×10^{-4} in the near-wall region and 1 to 2×10^{-3}. Here, the higher values

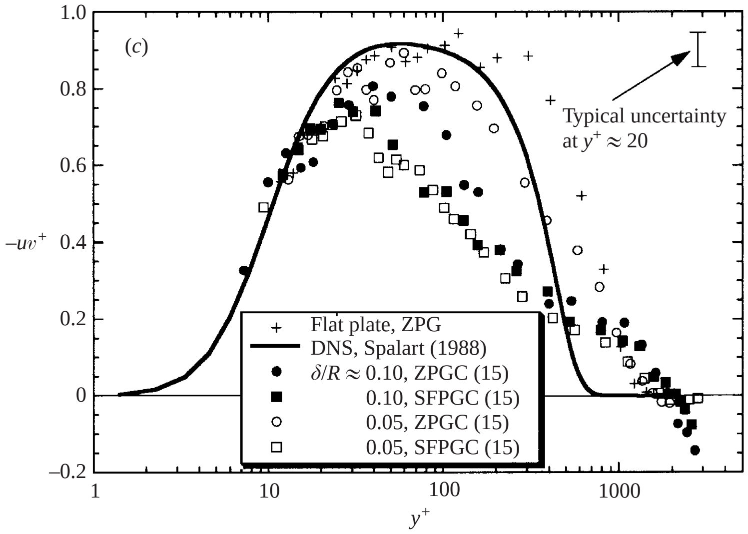

FIGURE 18. Profiles of (*a*) streamwise and (*b*) wall-normal r.m.s. velocity (typical uncertainty of the order of plot symbol size); and (*c*) primary Reynolds shear stress profiles for TS1 and TS2 under different streamwise pressure gradient conditions at $\alpha \approx 15°$.

for the ratio of normal to mean shear production are present when combining with strong convex curvature through almost the entire boundary layer.

In figure 17, the inner-normalized mean streamwise velocity distributions are shown. In all cases, the extent of the log-law region is reduced owing to the presence of the radial pressure gradient, which also increases the wake component in the outer portion of the TBL with respect to flat-plate results. The largest increase of the wake component occurred for ZPG, especially for the moderate curvature case. This behaviour is primarily attributed to the higher local acceleration near the onset of curvature for the strong curvature (see figure 5) case causing a reduction in the wake component. In addition, the streamwise distance is $s - s_0 \approx 2.6\delta_0$ for TS1 and $s - s_0 \approx 5.2\delta_0$ for TS2, resulting in a longer development distance from the onset of curvature for the case with moderate curvature and hence more time for the wake component to develop. On the other hand, the strong FPG had the tendency to oppose the wake-enhancing effect of the stabilizing curvature. This effect was more pronounced in the moderate curvature case, whereas in the presence of strong convex curvature, the reduction of the wake component relative to the corresponding ZPG case was minimal. In each of these cases, inner variable scaling accounts for the effects of multiple strain rates in the inner region, and the mean velocity profiles collapse. The largest deviations are observed in the outer portion of the TBL, where inner scaling is not expected to apply.

The streamwise and wall-normal r.m.s. velocities, along with the primary Reynolds shear stress component, shown in figure 18, further illustrate the effects of the extra strain rates. The streamwise r.m.s. velocity component data, shown in figures 18(*a*) and 18(*b*), collapse well in the near-wall region ($y^+ \leqslant 50$), whereas the effects of curvature combined with various streamwise pressure gradients are more pronounced in the outer portion of the boundary layer. For both curvature cases, the streamwise velocity fluctuation is reduced in the presence of favourable pressure gradients relative to the ZPG cases, and this reduction is greater for the weaker convex curvature, where the axial pressure gradient is ‘stronger’ relative to that in the strong curvature case.

For both curvatures, the FPGs enhance the stabilizing effect of the convex curvature in the sense that the Reynolds stresses are suppressed. For the wall-normal r.m.s. component, these differences occur throughout the entire boundary layer and the trends are consistent with the observations made for the streamwise component.

The various profiles of the primary Reynolds shear stress, $-\overline{uv}$, are shown in figure 18(*c*), where the effects of the different interacting pressure gradients are obvious. The imposed favourable streamwise pressure gradient further reduces $-\overline{uv}$ throughout most of the TBL, for both curvature cases. It is noteworthy that the reduction in the outer portion ($y^+ \geqslant 50$) of the boundary layer is greater for the moderate curvature case when comparing ZPG and strong FPG. The effects of the different strengths of curvature can also be observed in the outer portion of the Reynolds stress profiles. Comparing both ZPG cases with different curvature, the primary Reynolds shear stress is more suppressed for the stronger convex curvature, indicating that the destruction of the energy-containing eddies is more advanced. As mentioned before, this effect was demonstrated by Chiwanga & Ramaprian (1993), who showed that the destruction of large-scale structures in the outer portion of the TBL was due to the strong stabilizing convex curvature.

4.3. *Production terms*

In order to examine the effects of different combination of strain rates, i.e. different magnitudes of the pressure gradient ratio on selected measured Reynolds stress terms, the dominant production terms for the streamwise normal Reynolds stress and the primary Reynolds shear stress were calculated. For a curved boundary layer, these terms are:

$$\mathrm{Prod}\left(\frac{\overline{u^2}}{2}\right) = \underbrace{-\overline{uv}\,h\frac{\partial \bar{U}}{\partial y}}_{\text{Mean shear production}} + \underbrace{\overline{uv}\,\frac{\bar{U}}{R}}_{\text{Curvature production}} - \underbrace{\overline{u^2}\frac{\partial \bar{U}}{\partial s}}_{\text{Normal stress production}} \underbrace{-2\overline{uv}\,\frac{\bar{U}}{R}}_{\text{Coordinate rotation}}, \tag{14a}$$

$$\mathrm{Prod}(-\overline{uv}) = \underbrace{\overline{v^2}\,h\frac{\partial \bar{U}}{\partial y}}_{\text{Mean shear production}} - \underbrace{\overline{u^2}\frac{\bar{U}}{R}}_{\text{Curvature production}} \underbrace{-[\overline{u^2}-\overline{v^2}]\frac{\bar{U}}{R}}_{\text{Coordinate rotation}}, \tag{14b}$$

where $h = 1 + y/R$, and y is the wall-normal coordinate, often designated by n. The production terms in the turbulent kinetic energy are as follows:

$$\mathrm{Prod}\left(\frac{\overline{q^2}}{2}\right) = \underbrace{-\overline{uv}\,h\frac{\partial \bar{U}}{\partial y}}_{\text{Mean shear production}} + \underbrace{\overline{uv}\,\frac{\bar{U}}{R}}_{\text{Curvature production}} - \underbrace{[\overline{u^2}-\overline{v^2}]\frac{\partial \bar{U}}{\partial s}}_{\text{Normal stress production}}. \tag{14c}$$

Note that the strain rates associated with the streamwise gradient affect the transport equations through the terms labelled ‘normal stress production’. These terms are obtained from the Reynolds stress transport equations given by Bradshaw (1973) after applying continuity to replace $\mathrm{d}V/\mathrm{d}y$, as suggested by Baskaran *et al.* (1991). The importance of anisotropy is obvious in the normal stress production of $\overline{u^2}$ and turbulent kinetic energy (equations (14*a*) and (14*c*)).

Production terms for $\overline{u^2}$ and $-\overline{uv}$ are plotted in figure 19, using inner normalization. They are compared with the measured flat plate data and the DNS data of Spalart (1988). The profiles for the production of the streamwise normal Reynolds stress (figure 19*a*) are identical to each other and to the flat plate data throughout the entire

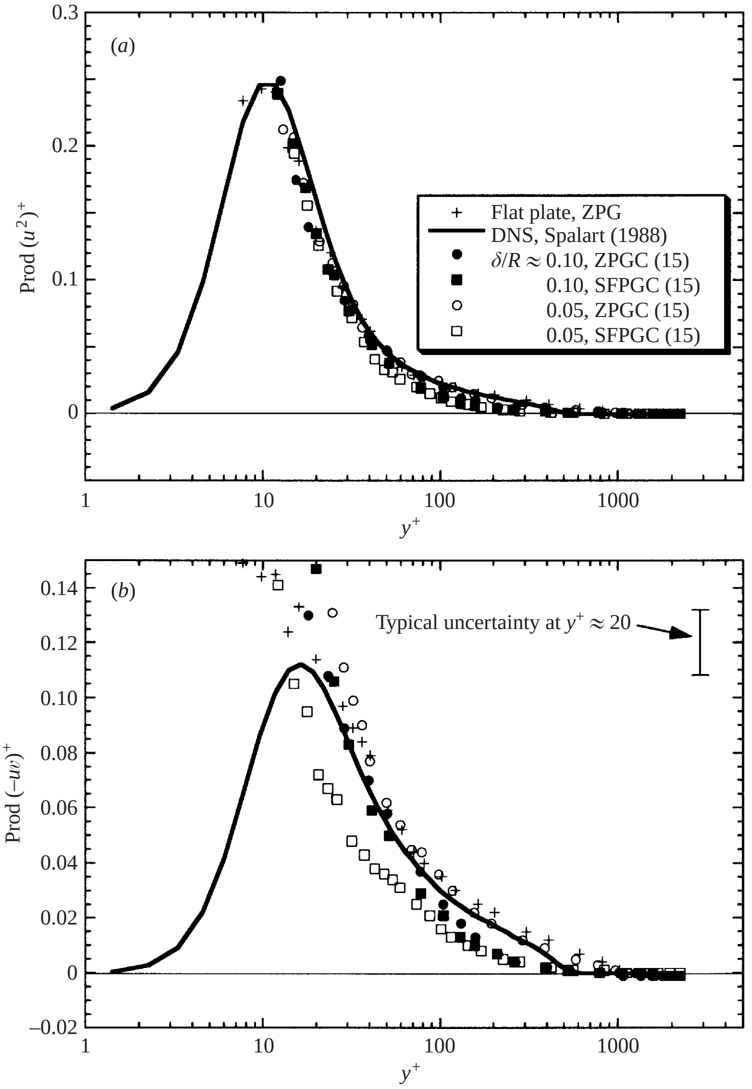

FIGURE 19. Production of (*a*) normal and (*b*) primary shear Reynolds stress for TS1 and TS2 under different streamwise pressure condtions (uncertainty of the order of plot symbol size in (*a*)).

boundary layer. Small differences are noticeable outside the log-law region, where streamwise favourable pressure gradient augments the stabilizing effect of the convex curvature, as already seen in the Reynolds stresses (figure 18). On the other hand, the production for the primary Reynolds shear stress, shown in figure 19(*b*), is reduced in the same portion of the boundary layer as that in which the primary Reynolds shear stress is reduced.

Combined with the previous observations, the data indicate that the effects of the applied extra rates-of-strain on the near-wall region of the turbulent boundary layer are completely scaled by changes in u_τ, and that the flow field is most obviously affected in the outer portion of the boundary layer. It will be shown in §4.4 that the turbulence bursting period shows significant changes for the different cases discussed, hence these results suggest that the bursting phenomenon is controlled by the dynam-

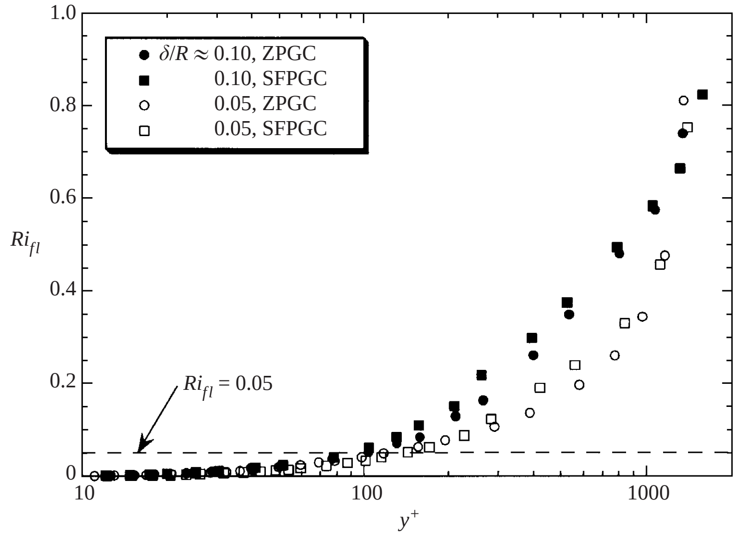

FIGURE 20. Streamwise development of flux Richardson number for strong and moderate convex curvature under ZPGC and SFPGC conditions at $\alpha \approx 15°$ (uncertainty of the order of plot symbol size).

ics of the entire boundary layer. Furthermore, they imply that the production cycle mechanisms are closely coupled with the applied strain rates.

The variation of the flux Richardson number, which gives additional insight into streamline curvature effects on a turbulent boundary layer and its implications on the structural changes inside the TBL are shown in figure 20. In this figure, the flux Richardson number is shown for both curvature cases subject to ZPGC and SFPGC at $\alpha \approx 15°$. For all profiles shown, Ri_{fl} exceeds its critical value of 0.05 (Townsend 1976) at $y^+ \approx 100$, the upper limit of the log-law region. This supports our previous statement that the outer portion of the TBL was more strongly affected by the extra strain rates. The relative increase of the flux Richardson number for the strong convex curvature case compared to the moderate curvature case is consistent with the elevated stabilizing effect on the TBL in the presence of stronger convex curvature. On the other hand, different strengths of favourable pressure gradients yield a smaller increase in Ri_{fl}. Consequently, it appears that the strong radial pressure gradient due to wall curvature is the dominant pressure gradient in this flow field.

4.4. *Burst frequencies*

In figure 21, the mean burst frequency normalized with inner variables ($\bar{f}_B^+ = \bar{f}_B \nu / u_\tau^2$) is shown for both curvature cases as a function of the streamwise distance along the convex wall for ZPG, FPG, and APG. For the strong curvature case (figure 21*a*), the burst frequency was reduced immediately downstream of the onset of curvature, and even further reduced in the presence of favourable pressure gradients. On the other hand, it was increased for the adverse pressure gradient, indicating a more frequent occurrence of these events. The same trends were also observed for mixed and outer normalization of the burst frequency (Schwarz & Plesniak 1996*a*). The (inner normalized) burst frequency was 18% smaller at $\alpha \approx 15°$ for the strongest FPG case (SFPG) compared to the ZPG case. In addition, the duration of ejections became shorter in the presence of SFPG. The (inner normalized) duration times for ejections at four different stations for all streamwise pressure gradients are given in

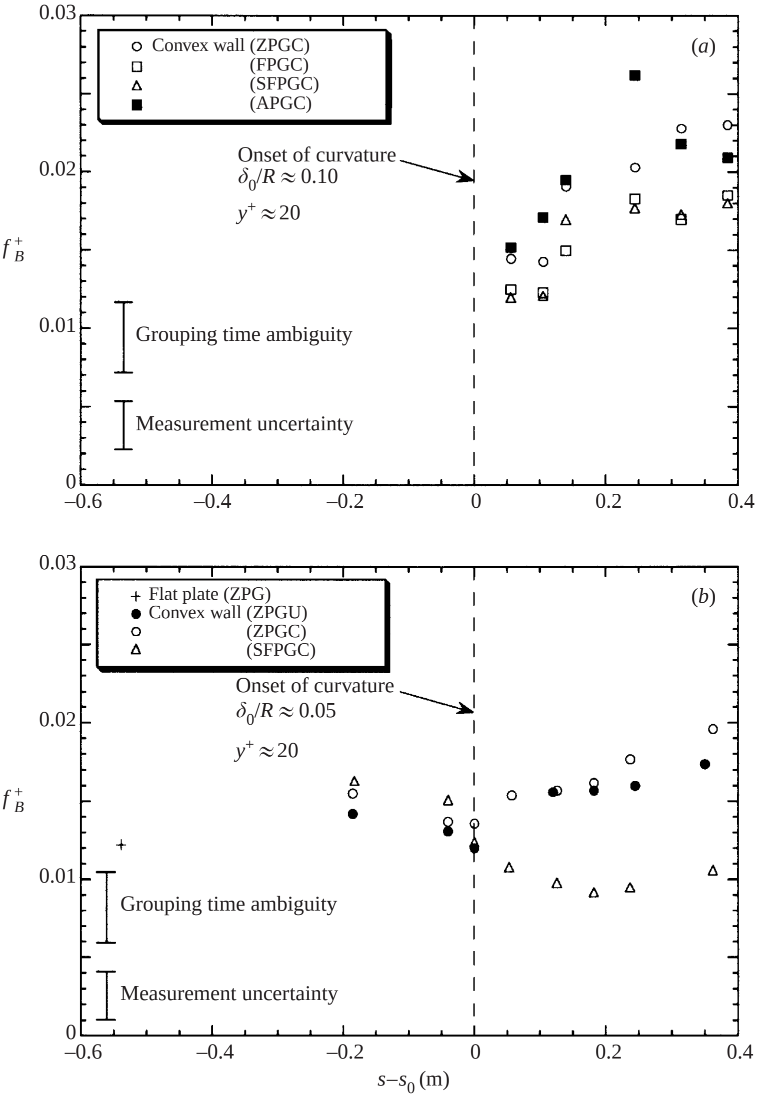

FIGURE 21. Streamwise distribution of inner normalized burst frequency for (*a*) TS1 and (*b*) TS2 under different streamwise pressure conditions.

table 4, which clearly shows that the duration decreases in the presence of favourable streamwise pressure gradients. The values shown in table 4 correspond to a particular threshold value of $H = 0.2$, but the trends are the same for the entire threshold-independent range. Thus, because bursts are less frequent and of shorter duration downstream of the initial region ($\alpha \geqslant 20°$), FPG in the convex turbulent boundary layer is associated with a suppression of the turbulence production cycle. Although the difference in the (inner-normalized) burst frequency decreased with downstream distance, the combination of the strong curvature with strong FPG resulted in an increased stabilization of the turbulent boundary layer throughout the measurement domain (28% reduction of burst frequency at 55°).

On the other hand, the interaction of the strong convex curvature with APG had the opposite effect. Especially in the initial curved wall region (but even up to $\alpha \approx 35°$),

(*a*)	Case	$\alpha \approx 15°$	$\alpha \approx 20°$	$\alpha \approx 35°$	$\alpha \approx 55°$	
	APG	1.45	1.70	1.71	1.78	
	ZPG	1.95	2.17	2.33	2.13	
	FPG	2.05	2.02	2.18	2.13	
	SFPG	1.68	1.88	2.04	2.07	
(*b*)	Case	$\alpha \approx 0°$	$\alpha \approx 10°$	$\alpha \approx 15°$	$\alpha \approx 20°$	$\alpha \approx 30°$
	ZPGU	2.43	2.12	1.94	1.83	1.49
	ZPGC	2.13	1.87	1.93	1.83	1.75
	SFPG	2.16	1.64	1.73	2.02	1.56

TABLE 4. Inner normalized ejection duration $\Delta\tau_E^+ = \Delta\tau_E u_\tau^2/\nu$ for different streamwise pressure gradients ($H = 0.2$) with (*a*) $\delta_0/R \approx 0.10$, (*b*) $\delta_0/R \approx 0.05$.

the burst frequency was elevated relative to the ZPG values. In any case, the turbulent burst frequency is low in the initial region, immediately downstream of the onset of curvature, which is attributed to the sudden change in surface curvature. However, in the presence of APG, the ejection duration is reduced compared to all other cases along the entire test surface, as shown in table 4(*a*). This behaviour can be linked to the initially strong application rate of the streamwise strain rate (figure 5), causing a reduction in the duration of uv_2 events, accompanied by a more frequent occurrence of the bursting events. These results imply that not only the magnitude, but also the rate of application of the strain rate, dictates the state of the turbulence throughout the measurement domain. In summary, APG is associated with increased turbulence production, which coincides with an increase of the primary Reynolds shear stress, despite the fact that the ejection duration of the detected events is reduced.

In figure 21(*b*), the burst frequencies for the moderate curvature case are shown. Also included is the value for the upstream flat-plate reference station. In this case, data are shown for three different streamwise pressure gradient distributions, two zero (compensated and uncompensated) and strong favourable pressure gradient (SFPG). The uncompensated zero pressure gradient (ZPGU) exhibits a stronger local acceleration at the onset of curvature compared to the compensated case (ZPGC), because the flexible wall opposite the measurement wall was not corrected to counteract the initial acceleration. As in the strong curvature case, the burst frequency is reduced near the onset of curvature owing to the stabilizing nature of the local favourable pressure gradient. The burst frequency increases monotonically downstream for both ZPGs. On the other hand, a dramatic decrease in f_B occurs initially in the presence of the SFPG, reaching a minimum at $\alpha \approx 15°$. This trend is completely opposite to that observed for the strong curvature case, where the burst frequency increased monotonically after reaching a minimum value immediately downstream of the onset of curvature. In comparison with figure 21(*a*), it is evident that the turbulence production cycle experiences a higher suppression when SFPG and moderate curvature are combined. Recall that the ratio of the streamwise (SFPG) to radial pressure gradient P_{rat} is 1.2 for the moderate and 0.6 for the strong convex curvature.

The inner-normalized duration of ejection events for the moderate curvature data, shown in table 4, generally support the bursting frequency trends. In general, the ejection duration is shorter in the presence of SFPG than for either ZPG case. This indicates that the strong favourable pressure gradient has a stabilizing effect on the

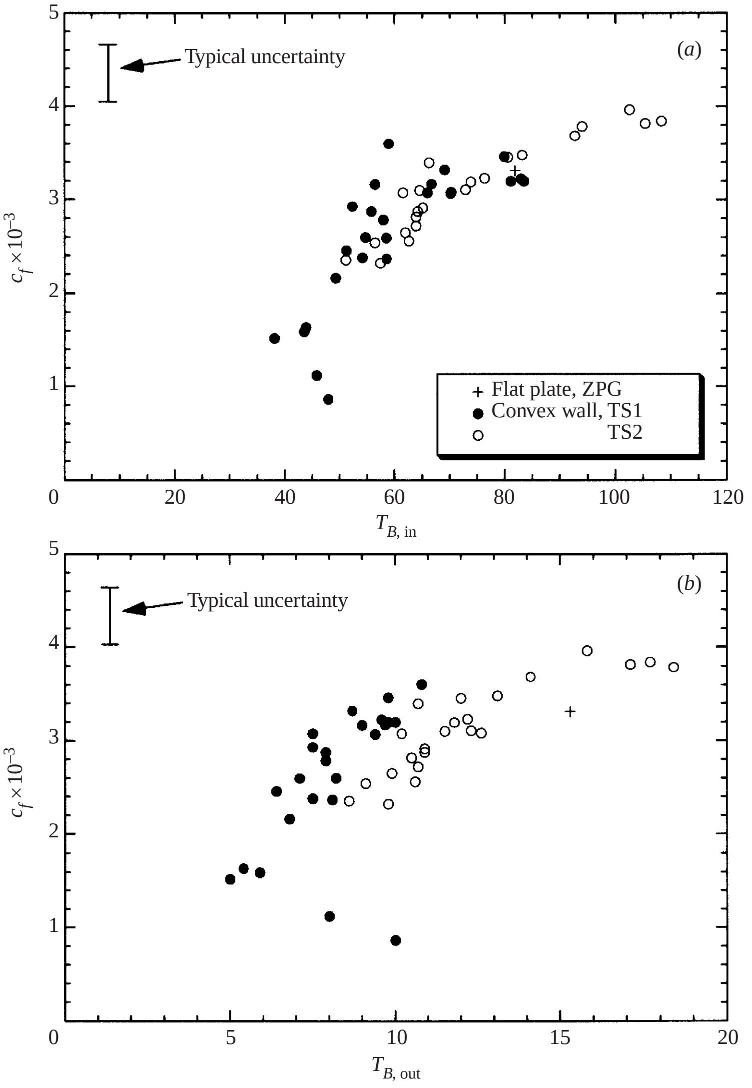

FIGURE 22. Skin-friction coefficient as a function of the (*a*) inner and (*b*) outer normalized bursting period for TS1 and TS2.

turbulent boundary layer when combined with a more moderate convex curvature and it is in good agreement with the Reynolds stress measurements (figure 18).

4.5. *Effects of combined strain rates*

To further examine the effect of combined strain rates on the turbulence structure, we attempted to identify correlations between a standard integral parameter (i.e. wall-shear stress or skin-friction coefficient) and the bursting period. These parameters were chosen because of the relevance of the wall-shear stress and the importance of the frequency of the main Reynolds-stress-producing event for modelling considerations. The burst period using inner (figure 22*a*) and outer normalization (figure 22*b*) as a function of the skin-friction coefficient is shown for all applied streamwise pressure gradients and curvatures. The main observation that can be drawn from this figure

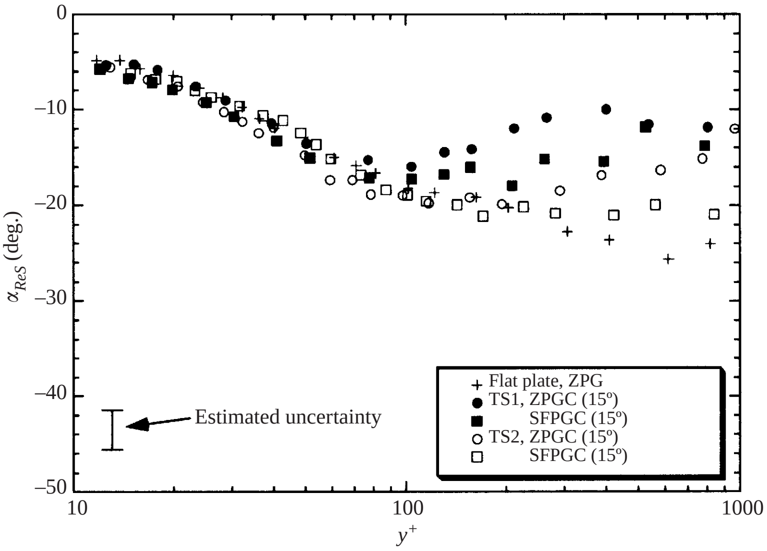

FIGURE 23. Angle of principal axes of the Reynolds stress tensor with different pressure gradient ratios.

is the monotonically increasing bursting period (reduction of the bursting event frequency) with increasing skin-friction. This result implies that the normalized bursting period is simply related to the skin-friction coefficient, independent of whether the TBL develops over a flat plate with ZPG or whether it is exposed to multiple extra rates-of-strain.

In figure 23, the principal axes for the Reynolds stress tensor are shown for the data sets discussed in § 4.2 to illustrate the effect of different strain rate ratios on the structural features of the boundary layer. The distribution of the principal axes of the strain rate tensor are omitted here, owing to a high ‘noise’ level, which results after differentiating the velocity data. However, for a plane constant shear, the principal axis is $\alpha_{SR} = 45°$, and our results are in that neighbourhood (Schwarz 1998). For non-homogeneous turbulence, the principal axes of the Reynolds stress tensor are not aligned with those of the strain rate tensor (Gence & Mathieu 1979). The angle of the principal axes of the Reynolds stresses can be interpreted as an indirect measure for how well the velocity fluctuations in the streamwise and wall-normal direction are correlated with each other, and also the degree to which the flow is locally isotropic, i.e. $\overline{u^2} - \overline{v^2} \Rightarrow 0$. Both trends would increase the magnitude of the Reynolds stress principal axes. The Reynolds stress principal axes angle, α_{ReS} shown in figure 23 is unaffected by the interacting strain rates inside the log-law region ($y^+ \leqslant 100$). In the outer portion of the TBL, the ZPGC case with strong convex curvature (TS1) shows the largest reduction of α_{ReS} relative to flat-plate values. This behaviour is consistent with the highest local application rate of newly introduced strain rates especially in the streamwise direction (figure 5). It can be expected that the Reynolds stress principal axes is not aligned with the strain rate tensor’s principal axes, especially in the outer portion of the boundary layer, which is a violation of the Boussinesq approximation. One of the major shortcomings of standard turbulence models (e.g. k–ε model) applied to the current flow is the use of an isotropic scalar eddy viscosity even though the turbulence has strong non-isotropic features.

To further demonstrate the behaviour of α_{ReS} its streamwise evolution immediately

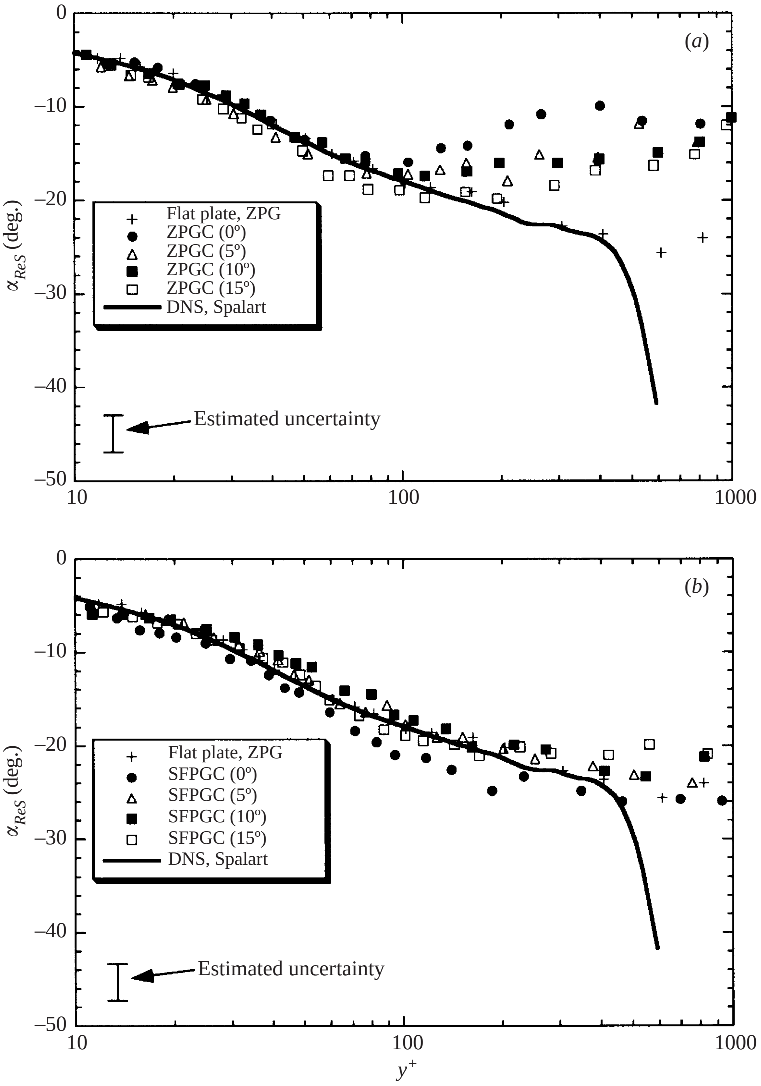

FIGURE 24. Angle of the Reynolds stress tensor principal axes for TBL with (*a*) compensated zero and (*b*) strong favourable streamwise pressure gradient. $\delta/R \approx 0.05$.

downstream of the onset of curvature for ZPGC and SFPGC in TS2 is shown in figure 24. Here, the angle of the principal Reynolds shear stress tensor axes is immediately suppressed for the ZPGC case (figure 24*a*), but remains essentially unchanged for the SFPGC case (figure 24*b*). The same trend for a zero-pressure-gradient turbulent boundary layer forming over a convex wall was predicted by Hong & Murthy (1986*b*), who developed the large eddy interaction model (LEIM), a finite velocity transport approach which is an alternative to the more frequently used simple gradient diffusion hypothesis. They found that the angle of the principal axes of the stress decreased with convex curvature. As before, the TBL for the ZPGC case is exposed to a rapidly changing application rate of streamwise acceleration or deceleration causing α_{ReS} to be reduced. These results further demonstrate that the

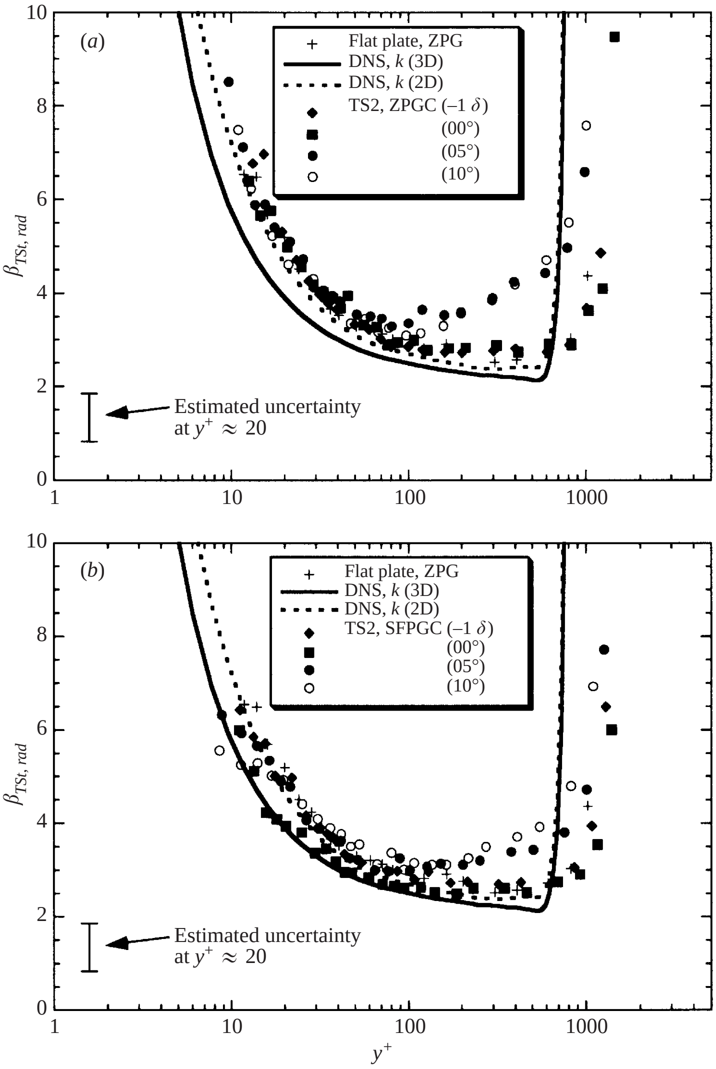

FIGURE 25. Total strain parameter for TBL with (*a*) compensated zero and (*b*) strong favourable streamwise pressure gradient for TS2. $\delta/R \approx 0.05$.

rate of application of the newly applied strain rates is at least as important as the magnitude of the strain rates itself.

In figure 25, the estimated total strain parameter, which can be used to determine whether the flow should be treated as a rapidly distorting flow, is shown as a function of the inner-normalized wall-normal coordinate for the initial region in TS2 under ZPGC (figure 25*a*) and SFPGC (figure 25*b*) conditions. The profiles for the flat plate and the DNS data sets using two-dimensional (2D) and three-dimensional (3D) representations of turbulent kinetic energy, k are included for comparison. There is good agreement between all data sets for the inner near-wall region, as seen previously. Outside the log-law region ($y^+ \geqslant 100$), the total strain parameter becomes elevated as soon as the flow enters the curved portion of the test section. This trend is consistent for all of the applied streamwise strain rates.

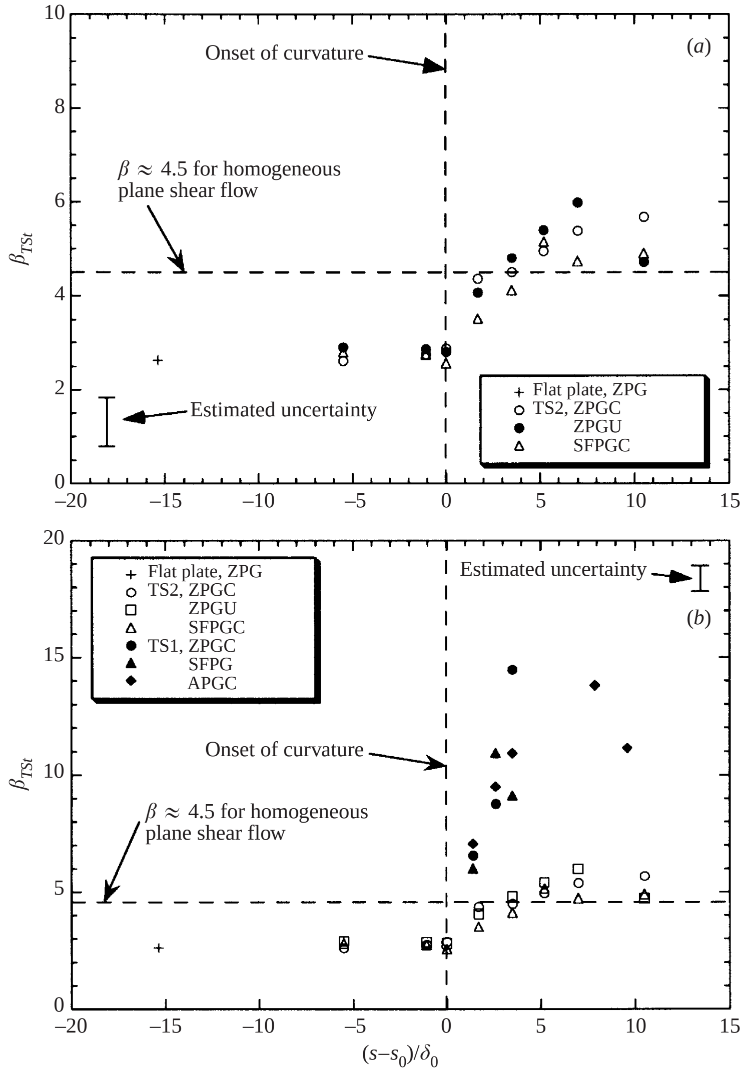

FIGURE 26. Streamwise variation of the total strain parameter for (*a*) TS2 and (*b*) TS1 and TS2 combined in the outer portion of the TBL.

In order to gain a better understanding, the streamwise variation of the total strain parameter in the outer portion of the boundary layer is examined ($y/\delta \approx 0.4$ as suggested by Sreenivasan 1985). Figure 26 shows the streamwise development under different conditions, i.e. moderate convex curvature (TS2) with different streamwise pressure gradient in figure 26(*a*), and both curvature cases with zero, favourable and adverse (only for TS1) streamwise pressure gradients in figure 26(*b*). The trends are striking. For both curvature cases, the total strain parameter is elevated immediately downstream of the onset of curvature, relative to the flat-plate values. Note that the equilibrium value for homogeneous plane shear flow is approximately 4.5 (see Sreenivasan 1985). However, this value is magnified by approximately a factor of 4 for the strong curvature case. It is still questionable whether or not the flow reaches a new, higher total strain parameter (approximately 5.5 for TS2 and 13.0 for TS1), especially in the case of strong convex curvature. This information would be valuable in assessing the modified turbulence structure for curved boundary-layer flows.

The following interpretation of these results is proposed. The nonlinear cascade process describes the interaction of the eddies of different size, where it is assumed that the large energy-containing eddies lose their energy to somewhat smaller eddies, which in turn lose their energy to still smaller eddies all the way down to the smallest scale eddies, which finally dissipate the energy by viscous interaction. It is this last stage that is described by the isotropic dissipation rate ε, which is an integral part of a variety of turbulent models (see van den Berg 1984). However, the rate of dissipation is determined by the first few stages of the cascade process, i.e. by the large eddies. In addition, the effectiveness at which the large eddies extract energy from the mean shear flow is believed to be linked to how well the principal axes of vorticity are aligned with those of the mean strain rate (Tennekes & Lumley 1972). Any mechanism that would suppress or even inhibit the initial stage in the nonlinear cascade process, or any mechanism that would affect the dynamic interaction between the turbulence and the mean flow, would instantly result in a variation of ε, which would cause the total strain parameter to change.

In a direct numerical simulation (DNS) of an elliptical shear flow by Blaisdell & Shariff (1996), which combines a homogeneous turbulent flow with the effects of solid-body rotation and strain, it was found that the nonlinear cascade process was suppressed for early times. This effect was enhanced for stronger rotation, whereas it recovered as the flow field developed further in time. The relationship to the present results is as follows. The newly applied extra rates of strain at the onset of curvature have a significant effect on the turbulence structure of the developing boundary layer. Immediately downstream of the onset of curvature, the turbulence production cycle is inhibited and the total strain parameter is elevated. Equation (15) shows how the total strain parameter is related to the TKE and the turbulence dissipation rate:

$$\beta_{TSt} \propto \frac{\frac{1}{2}\overline{q^2}}{\varepsilon}\frac{\partial \bar{U}}{\partial y}. \tag{15}$$

Since the data show that neither the TKE nor the mean shear rate are significantly altered when the additional strains are imposed, the increase in β_{TSt} results from a reduction of the turbulence dissipation rate ε. This implies that the nonlinear cascade transfer process is inhibited or the dynamic interaction between the turbulence and the mean flow is affected by the sudden introduction of extra strain rates. Detailed spectral measurements are necessary to examine these mechanisms further.

5. Summary and conclusions

Experiments have been carried out in a low-speed water tunnel to demonstrate the response of a turbulent boundary layer to the application of multiple pressure gradients. Constant pressure gradient boundary layers were established downstream of the onset of curvature for two different curved test sections (strong and moderate curvature).

The geometric configuration studied was representative of relatively low-aspect-ratio turbine vane passages. The emphasis of the study was on the near-wall inner layer of the convex wall boundary layer subjected to various pressure gradients. The initial region of curvature, where the turbulence is not in equilibrium, was measured extensively, and the degree of relaxation back to equilibrium was examined. Novel near-wall data as well as bursting information are reported.

The response of the turbulent boundary layer to multiple, combined strain rates (here radial and streamwise pressure gradients) was reflected in several different measured and deduced quantities. It is evident that both extra rates-of-strain have an effect on the mean and fluctuating features of the flow field, i.e. the skin-friction coefficient experienced the counteracting effect of the favourable pressure gradient to the radial strain. This behaviour and the response of other TBL quantities (i.e. strength of wake, Reynolds stresses, bursting period, equilibrium considerations) to the applied strains clearly indicate that the applied pressure gradients interact with each other. The interaction is not a simple one that is linearly superposable, but rather there is a mutual nonlinear interaction, which produces some net effect.

It was confirmed that convex curvature for zero pressure gradient, causes a dramatic reduction of the primary Reynolds shear stress in the outer portion of the boundary layer compared to turbulent flow over a flat plate, which can be attributed to the destruction of the large eddies owing to convex curvature. Favourable pressure gradients augmented the stabilizing curvature effects, whereas adverse pressure gradient counteracted that trend.

The convex turbulent boundary layer reaches a state of similarity at approximately $8\delta_0$ downstream of the onset of curvature. Favourable pressure gradient, when interacting with convex curvature, opposes the wake-enhancing effect of the convex curvature but augments its stabilizing effect on the turbulent stresses and transport. On the other hand, adverse pressure gradient enhances the wake strength but it counteracts the stabilizing effect of convex curvature.

As the flow develops downstream of the onset of curvature, there is an immediate response of the turbulence momentum transport, i.e. reduction of the primary Reynolds shear stress, especially in the outer region of the boundary layer ($y^+ > 70$). The higher strain rate ratio (strong FPG with moderate curvature, TS2) has an increased stabilizing effect on the turbulent boundary layer.

The turbulence production cycle is suppressed at the onset of curvature in all cases owing to a local acceleration of the boundary layer. In the case of SFPG interacting with moderate convex curvature (higher strain rate ratio, $P_{rat} = 1.2$ for moderate curvature, compared to 0.6 for strong convex curvature), the production cycle becomes suppressed even more, as reflected in an increase of the burst period. The burst measurements also emphasize the importance of the application rate of the newly applied strain rate. This feature, along with the strength and the relative magnitude of the interacting strains, must be considered in an attempt to develop a reliable model for this type of complex flow field. Along with an abrupt suppression of the turbulence production cycle, the total strain parameter, which is a measure for the average life-time of the large, energy-containing eddies, increases immediately after introduction of convex curvature. Because the production of turbulence energy occurs mainly in the near-wall region, and the large eddies exist in the outer layer, it is concluded that the sudden introduction of multiple extra strain rates affects the turbulence structure of the entire boundary layer.

Perhaps most significantly, we have found that the response of a turbulent shear flow to more than one additional rate of strain is dependent on the rate of application of the different strain rates, and this is evident in the effect on the turbulence energy redistribution. The apparent dominance of one applied rate of strain over another (in a given context) is also dependent on the rate of application of the two strain rates, as well as their magnitudes. The results presented in § 4 clearly show the nonlinear nature of combining rates of strain, and their net effect is not predictable from any simple stress–strain rate law. Even the smallest second additional rate of strain (and its application rate) has a large effect in the vicinity of the application, where the ‘vicinity’ in question may not be small.

Further study is required to understand precisely how the strain rates combine with respect to any turbulence feature and the reason for the dominance of one over the other.

This work was sponsored by the Air Force Office of Scientific Research, Air Force Material Command, USAF, under grant number F 49620-93-1-0003. The US Government is authorized to reproduce and distribute reprints for Governmental purposes notwithstanding any copyright notation thereon.

REFERENCES

Bandyopadhyay, P. R. & Ahmed, A. 1993 Turbulent boundary layers subjected to multiple curvatures and pressure gradients. *J. Fluid Mech.* **246**, 503.

Barlow, R. S. & Johnston, J. P. 1985 Structure of turbulent boundary layers on a concave surface. *Stanford University Rep.* MD-47.

Barlow, R. S. & Johnston, J. P. 1988*a* Structure of turbulent boundary layers on a concave surface. *J. Fluid Mech.* **191**, 137.

Barlow, R. S. & Johnston, J. P. 1988*b* Local effects of large-scale eddies on bursting in a concave boundary layer. *J. Fluid Mech.* **191**, 177.

Baskaran, V., Smits, A. J. & Joubert, P. N. 1987 A turbulent flow over a curved hill. Part 1. *J. Fluid Mech.* **182**, 47.

Baskaran, V., Smits, A. J. & Joubert, P. N. 1991 A turbulent flow over a curved hill. Part 2. *J. Fluid Mech.* **232**, 377.

van den Berg, B. 1984 Production of turbulence according to the transport equations. National Aerospace Laboratory NLR Report, MP 84030 U.

Blackwelder, R. F. & Kaplan, R. E. 1976 On the bursting phenomenon near the wall in bounded shear flows. *J. Fluid Mech.* **76**, 89.

Blaisdell, G. A. & Shariff, K. 1996 Simulation and modeling of the elliptic streamline flow. *Center for Turbulence Research, Proceedings of the Summer Program 1996.*

Bogard, D. G. 1982 Investigation of burst structures in turbulent channel flows through simultaneous flow visualization and velocity measurements. PhD thesis, Purdue University, West Lafayette, IN.

Bogard, D. G. & Tiederman, W. G. 1986 Burst detection with single-point velocity measurements. *J. Fluid Mech.* **162**, 389.

Bradshaw, P. 1969 The analogy between streamline curvature and buoyancy. *J. Fluid Mech.* **36**, 177.

Bradshaw, P. 1973 Effects of streamline curvature on a turbulent flow. *AGARDograph* 169.

Bradshaw, P. 1994 Turbulence: the chief outstanding difficulty of our subject. *Exps. Fluids* **16**, 203.

Chebbi, B., Holloway, A. G. L. & Tavoularis, S. 1998 The response of sheared turbulence to changes in curvature. *J. Fluid Mech.* **358**, 223.

Chiwanga, S. C. & Ramaprian, B. R. 1993 The effect of convex wall curvature on the large-scale structure of the turbulent boundary layer. *Exp. Thermal Fluid Sci.* **6**, 168.

Fernholz, H. H. & Warnack, D. 1998 The effects of favourable pressure gradient and of the Reynolds number on an incompressible axisymmetric boundary layer. Part 1. The turbulent boundary layer. *J. Fluid Mech.* **359**, 329.

Gence, J. N. & Mathieu, J. 1979 On the application of successive plane strains to grid-generated turbulence. *J. Fluid Mech.* **93**, 501.

Gibson, M. M. 1984 Effects of streamline curvature on turbulence. In *Frontiers in Fluid Mechanics* (ed. S. H. Davis & J. L. Lumley), pp. 184–198. Springer.

Gibson, M. M. 1988 Effects of surface curvature on the law of the wall. In *Near-wall Turbulence*, 1988 Zoran Zaric Memorial Conference (ed. S. J. Kline & N. H. Afgan), Hemisphere.

Gibson, M. M. Verriopoulos, C. A. & Vlachos, N. S. 1984 Turbulent boundary layer flow on a mildly curved convex wall surface. *Exps. Fluids* **2**, 17.

Gillis, J. C. & Johnston, J. P. 1983 Turbulent boundary layer flow and structure on a convex and its redevelopment on a flat wall. *J. Fluid Mech.* **135**, 123.

Holloway, A. G. L. & Tavoularis, S. 1998 A geometric explanation of the effects of mild streamline curvature on the turbulence anisotropy. *Phys. Fluids* **10**, 1733.

Hinze, J. O. 1975 *Turbulence*, 2nd edn, p. 75. McGraw-Hill.

Hong, S. K. & Murthy, S. N. B. 1986*a* Pressure–strain correlations in curved wall boundary layers. *AIAA J.* **24**, 361.

Hong, S. K. & Murthy, S. N. B. 1986*b* Effective velocity of transport in curved wall boundary layers. *AIAA J.* **24**, 971.

Kline, S. J. & McClintock, F. A. 1953 Describing uncertainties in single sample experiments. *Mech. Engng* **73**, 3–8.

Kline, S. J. Reynolds, W. C., Schraub, F. A. & Runstadler, P. W. 1967 The structure of turbulent boundary layers. *J. Fluid Mech.* **30**, 741.

Koskie, J. E. 1991 Turbulence structure and polymer drag reduction in adverse pressure gradient boundary layers. PhD thesis, Purdue University, West Lafayette, IN.

Liakopolous, A. 1984 Explicit representations of the complete velocity profile in a turbulent boundary layer. *AIAA J.* **22**, 844.

Lu, S. S. & Willmarth, W. W. 1973 Measurements of the Reynolds stress in a turbulent boundary layer. *J. Fluid Mech.* **60**, 481.

McLaughlin, D. K. & Tiederman, W. G. 1973 Biasing correction for individual realization of laser velocimeter measurements in turbulent flows. *Phys. Fluids* **16**, 2082.

Maxey, M. R. 1982 Distortion of turbulence in flows with parallel streamlines *J. Fluid Mech.* **124**, 261.

Moffat, R. J. 1988 Describing the uncertainties in experimental results. *Exp. Thermal Fluid Sci.* **3**, 3.

Moser, R. D. & Moin, P. 1987 The effects of curvature in wall-bounded turbulent flows. *J. Fluid Mech.* **175**, 479.

Muck, K. C., Hoffmanm, P. H. & Bradshaw, P. 1985 The effects of convex curvature on turbulent boundary layers. *J. Fluid Mech.* **161**, 347.

Nagano, Y., Tagawa, M. & Tsuji, T. 1991 Effects of adverse pressure gradients on mean flows and turbulence statistics in a boundary layer. *8th Symp. on Turbulent Shear Flows*, p. 2-3. University of Munich.

Narasimha, R. & Sreenivasan, K. R. 1979 Relaminarization of fluid flows. *Advances in Applied Mechanics*, vol. 19, p. 221. Indian Institute of Science, Bangalore, India.

Narayanan, M. A. B. & Ramjee, V. 1969 On the criteria for reverse transition in a two-dimensional boundary layer flow. *J. Fluid Mech.* **35**, 225.

Patel, V. C. 1997 Longitudinal curvature effects in turbulent boundary layers. *Prog. Aerosp. Sci.* **33**, 1.

Reynolds, W. C. & Kassinos, S. C. 1995 One-point modelling of rapidly deformed homogeneous turbulence. *Proc. R. Soc. Lond.* A **451**, 87.

Richman, M. S. 1994 Flow visualization in convex boundary layers with streamwise pressure gradients. Purdue University Internal Report, West Lafayette, IN.

Robinson, S. K. 1991 Coherent motions in the turbulent boundary layer. *Annu. Rev. Fluid Mech.* **23**, 601.

Runstadler, P. G., Kline, S. J. & Reynolds, W. C. 1963 An experimental investigation of flow structure of the turbulent boundary layer. *Rep. MD-8*. Dept Mech. Engng, Stanford University, Stanford, CA.

Savill, A. M. 1987 Recent developments in rapid-distortion theory. *Annu. Rev. Fluid Mech.* **19**, 531.

Schwarz, A. C. 1998 Response of a turbulent boundary layer to multiple strain rates. PhD thesis, Purdue University, West Lafayette, IN.

Schwarz, A. C. & Plesniak. M. W. 1996*a* The influence of interacting strain rates on turbulence in convex boundary layers. *Phys. Fluids* **8**, 3163.

Schwarz, A. C. & Plesniak, M. W. 1996*b* Convex turbulent boundary layers with zero and favourable pressure gradients, *Trans. ASME J. Fluids Engng* **118**, 787.

Shur, M. L., Strelets, M. K., Travin, A. K. & Spalart, P. R. 2000 Turbulence modeling in rotating and curved channels: Assessing the Spalart–Shur correction. *AIAA J.* **38**, 784–792.

Smits, A. J., Matheson, N. & Joubert, P. N. 1983 Low-Reynolds-number turbulent boundary layers in zero and favorable pressure gradients. *J. Ship Res.* **27**, 147.

So, R. M. C. & Mellor, G. L. 1973 Experiment on convex curvature effects in turbulent boundary layers. *J. Fluid Mech.* **60**, 43.

Spalart, P. R. 1988 Direct simulation of a turbulent boundary layer up to $Re_{\theta} = 1410$. *J. Fluid Mech.* **187**, 61.

Spalart, P. R. & Shur, M. 1997 On the sensitization of turbulence models to rotation and curvature. *Aerosp. Sci. Technol.* **1**, 297–302.

Sreenivasan, K. R. 1985 The effect of contraction on a homogenous turbulent shear flow. *J. Fluid Mech.* **154**, 187.

Tennekes, H. & Lumley, J. L. 1972 *A First Course in Turbulence*, pp. 6, 178. MIT Press.

Townsend, A. A. 1976 *The Structure of Turbulent Shear Flow*, 2nd Edn. Cambridge University Press.

Walker, D. T. & Tiederman, W. G. 1988 Turbulence structure and mass transport in a channel flow with polymer injection. Report PME-FM-88-2, Purdue University, West Lafayette, IN.

Webster, D. R., DeGraaff, D. B. & Eaton, J. K. 1996 Turbulence characteristics of a boundary layer over a two-dimensional bump. *J. Fluid Mech.* **320**, 53.

White, F. M. 1974 *Viscous Fluid Flow*, p. 478. McGraw-Hill.

White, J. B. & Tiederman, W. G. 1990 The effect of adverse pressure gradient on the turbulent burst structure in low-Reynolds number equilibrium boundary layers. *Proc. 12th Symp. on Turbulence, University of Missouri-Rolla, Rolla, MO*, p. A5.1.

Wu, X. H. & Squires, K. D. 1998 Numerical investigation of the turbulent boundary layer over a bump. *J. Fluid Mech.* **362**, 229.

Yanta, W. J. & Smith, R. J. 1973 Measurements of turbulence transport properties with a laser-Doppler velocimeter. *AIAA Paper* 73-169.